EUROPEAN LABORATORY FOR PARTICLE PHYSICS

OPAL Physics Note PN400
7th July 1999

Investigation of the Decay of Orbitally-Excited B Mesons and First Measurement of the Branching Ratio BR($B^*_J \to B^*\pi$)

The OPAL Collaboration

Abstract

From 4 million hadronic Z^0 decays recorded by the OPAL detector near the Z^0 resonance, we select a sample of more than 570 000 inclusively reconstructed B mesons. Orbitally-excited mesons B^*_J are reconstructed using $B\pi^\pm$ combinations. B^* mesons are reconstructed using the decay $B^* \to B\gamma$. The selected B^* candidates are used to obtain samples enriched or depleted in the decay $B^*_J \to B^*\pi^\pm$. From the number of signal candidates in the $B\pi^\pm$ mass spectra of these two samples, we perform the first measurement of the branching ratio of orbitally-excited B mesons decaying into B^*. The result is

$$\mathrm{BR}(B^*_J \to B^*\pi) = 0.85\,^{+0.26}_{-0.27} \pm 0.12\,,$$

where the first error is statistical and the second systematic.

This note describes preliminary OPAL results.

1 Introduction

An important prediction of Heavy Quark Effective Theory (HQET) is the existence of an approximate spin-flavour symmetry for hadrons containing one heavy quark Q ($m_Q \gg \Lambda_{\rm QCD}$) [1]. In the limit $m_Q \to \infty$, mesons composed of a heavy quark Q and a light quark q are characterised by the spin of the heavy quark S_Q, the total angular momentum of the light quark $j_q = S_q + L$ and the total angular momentum J, where S_q and L denote the spin and the orbital angular momentum respectively of the light quark. In the heavy quark limit, both S_Q and j_q are good quantum numbers and the total angular momentum of the meson is given by $J = S_Q + j_q$. For $L = 1$, there are four states with spin-parity $J^P = 0^+$, 1^+, 1^+ and 2^+. If the heavy quark Q is a bottom quark, these states are labelled B_0^*, B_1 for both 1^+ states[1] and B_2^* [2], respectively. The four states, commonly called B_J^*, or alternatively B^{**} [2], are grouped into two sets of degenerate doublets, corresponding to $j_q = 1/2$ and $j_q = 3/2$ as indicated in Table 1. Parity and angular momentum conservation put restrictions on the strong decays of these states to $\mathrm{B}\pi$ and $\mathrm{B}^*\pi$ (see Figure 1). The 0^+ state can only decay to $\mathrm{B}\pi$ via an S-wave transition, both 1^+ states can decay to $\mathrm{B}^*\pi$ via S-wave or D-wave transitions, and the 2^+ state can decay to both $\mathrm{B}\pi$ and $\mathrm{B}^*\pi$ only via D-wave transition. States decaying via an S-wave transition are expected to be much broader than the states decaying via a D-wave transition [4].

Given the HQET predictions listed in Table 1, the four B_J^* states are expected to overlap in mass. So far analyses at LEP [8–11] have reconstructed B_J^* in the $\mathrm{B}\pi$ final state only, observing one single peak in the $\mathrm{B}\pi$ mass spectrum. This is not sufficient to resolve any substructure of the four expected B_J^* states. In addition, for decays to $\mathrm{B}^*\pi$ where the photon in the decay $\mathrm{B}^* \to \mathrm{B}\gamma$ is not detected, the reconstructed $\mathrm{B}\pi$ mass is shifted by -46 MeV/c^2.

In this paper a different approach is presented. Using information of the photon in the decay $\mathrm{B}^* \to \mathrm{B}\gamma$, the $\mathrm{B}_J^* \to \mathrm{B}^*\pi^\pm$ transitions can be separated from the $\mathrm{B}_J^* \to \mathrm{B}\pi^\pm$ transitions. This allows a measurement of $\mathrm{BR}(\mathrm{B}_J^* \to \mathrm{B}^*\pi)$. Furthermore, this method gives insight into the decomposition of the B_J^* into the states allowed to decay to $\mathrm{B}\pi$ (B_0^* and B_2^*) from the other states that can only decay to $\mathrm{B}^*\pi$.

The paper is organised as follows: the next section describes the data sample and the event simulation. In Section 3, the analysis method is presented. In Section 4, the B reconstruction is described. Sections 5 and 6 contain the photon and pion reconstruction. Results are presented in Section 7 and systematic uncertainties are evaluated in Section 8. A discussion of the results and conclusions are given in Section 9.

2 Data sample and event simulation

The data used for this analysis were collected from $\mathrm{e}^+\mathrm{e}^-$ collisions at LEP during 1991–1995, with centre-of-mass energies at and around the peak of the Z^0 resonance. The data correspond to an integrated luminosity of about 140 pb^{-1}. A detailed description of the OPAL detector can be found elsewhere [12, 13].

Hadronic events are selected as described in [14], giving a hadronic Z^0 selection efficiency of $(98.4 \pm 0.4)\,\%$ and a background of less than $0.2\,\%$. A data sample of about 4 million hadronic events is selected. Each event is divided in two hemispheres by the plane perpendicular to the thrust axis and containing the interaction point of the event. The thrust axis is calculated

[1] In the case of mixing of the $J = 1$ states, the notation $\mathrm{B}_1(H)$ and $\mathrm{B}_1(L)$ is used to distinguish the physical states.

[2] Throughout this paper, we use the Particle Data Group notation B_J^* for orbitally-excited B mesons.

		predicted properties			Monte Carlo input	
state	J_j^P	mass [GeV] [3]	width [GeV] [4,5]	decay mode	mass [GeV]	width [GeV]
B_0^*	$0^+_{1/2}$	5.738	0.20-1.00	$(B\pi)_{S-wave}$	5.750	0.300
B_1	$1^+_{1/2}$	5.757	0.25-1.30	$(B^*\pi)_{S-wave}$	5.770	0.300
B_1	$1^+_{3/2}$	5.719	0.021	$(B^*\pi)_{D-wave}$	5.725	0.020
B_2^*	$2^+_{3/2}$	5.733	0.025	$(B^*\pi)_{D-wave}$, $(B\pi)_{D-wave}$	5.737	0.025

Table 1: Masses, widths and dominant decay modes based on theoretical predictions [3–7] and the corresponding Monte Carlo input values used in the analysis.

using charged tracks and electromagnetic clusters not associated with any tracks. To select events within the fiducial acceptance of the silicon microvertex detector and the barrel electromagnetic calorimeter, the thrust axis direction[3] is required to satisfy $|\cos\theta_T| < 0.8$. Monte Carlo simulated samples of inclusive hadronic Z^0 decays are used to evaluate efficiencies and backgrounds. The JETSET 7.4 parton shower Monte Carlo generator [15], with parameters tuned by OPAL [16] and with the fragmentation function of Peterson *et al.* [17] for heavy quarks is used to generate samples of approximately 10 million hadronic Z^0 decays, 2 million $Z^0 \to c\overline{c}$ and 5 million $Z^0 \to b\overline{b}$ decays. The generated events are passed through a program that simulates the response of the OPAL detector [18] before applying the same reconstruction algorithms as for data. All generated Monte Carlo samples contain $L = 1$ states for bottom and charmed mesons and the corresponding vector meson partners of the ground states. The generated production rates, masses and widths of all resonant states are consistent with experimental measurements where available and with theoretical predictions elsewhere (see also Table 1).

3 Analysis overview

The analysis is based on the reconstruction of B^* in the $B\gamma$ final state and a separate reconstruction of B_J^* in the $B\pi^\pm$ final state. A direct reconstruction of B_J^* decaying to $B^*\pi$, $B^* \to B\gamma$ giving $B\gamma\pi^\pm$ in the final state is inappropriate because of the large combinatorial background and the insufficient detector resolution. Therefore, our approach employs a statistical separation of $B_J^* \to B^*\pi$ from $B_J^* \to B\pi$ decays.

B mesons produced in $Z^0 \to b\overline{b}$ events are reconstructed inclusively to achieve high efficiency. No attempt is made to reconstruct specific B decay channels. On the contrary, properties common to all weakly decaying b hadrons are used for the B reconstruction. For each B candidate, a weight $\mathcal{W}(B^*)$ is formed. $\mathcal{W}(B^*)$ represents the probability for the B to have come from a B^*. $\mathcal{W}(B^*)$ is based on the reconstruction of photon conversions and of photons detected in the electromagnetic calorimeter. All B candidates are then combined with charged pions to form B_J^* meson candidates. Using the weight $\mathcal{W}(B^*)$, we derive two mutually exclusive subsamples of $B\pi^\pm$ combinations, one enriched and the other depleted in its B^* content. Invariant $B\pi^\pm$ mass distributions are formed for both samples. The shape of the non-B_J^* background of the

[3] In the OPAL coordinate system, the x axis points towards the centre of the LEP ring, the y axis points upwards and the z axis points in the direction of the electron beam. θ and ϕ are the polar and azimuthal angles, and the origin is taken to be the centre of the detector.

two distributions is taken from Monte Carlo simulation and normalised to the data in the upper sideband region and subtracted from the corresponding data distributions. From the observed number of B_J^* and the different efficiencies for $B_J^* \to B\pi^\pm$ and $B_J^* \to B^*\pi^\pm$ decays in the B^* enriched and the B^* depleted samples the branching ratio $BR(B_J^* \to B^*\pi)$ is obtained, as are some details of the B_J^* four-state composition.

In contrast to other measurements [11], this analysis does not make explicit use of HQET except for theoretical predictions that have already been confirmed by experimental results.

4 Selection and reconstruction of B mesons

B mesons are reconstructed using an extended version of the method used in earlier analyses [8, 19]. Since the reconstructed B mesons are used to form B^* and B_J^* candidates, the B reconstruction is tuned to minimise the uncertainties on the B direction and energy, while maintaining a high reconstruction efficiency.

4.1 Tagging of $Z^0 \to b\overline{b}$ events

To allow optimal b-tagging performance, each event is forced to a 2-jet topology using the Durham jet finding scheme [20]. In calculating the visible energies and momenta of the event and of individual jets, corrections are applied to prevent double counting of energy in the case of tracks with associated clusters [21]. A b-tagging algorithm is applied to each jet using three independent methods: lifetime tag, high p_T lepton tag and jet shape tag. A detailed description of the algorithm can be found in [22]. The b-tagging discriminants calculated for each of the jets in the event are combined to yield an event b likelihood $\mathcal{B}_{\rm event}$. For each event, $\mathcal{B}_{\rm event} > 0.6$ is required. After this cut, the $Z^0 \to b\overline{b}$ event purity is about 96%. The cut on the direction of the event thrust axis, $|\cos\theta_T| < 0.8$, as described in Section 2, removes roughly a quarter of all $Z^0 \to b\overline{b}$ events and after the cut on $\mathcal{B}_{\rm event}$, the total b event tagging efficiency with respect to all produced $Z^0 \to b\overline{b}$ events is about 49%, where these numbers are obtained from Monte Carlo simulation. At this stage, about 750 000 b hadron candidates are selected.

4.2 Reconstruction of B energy and direction

The primary event vertex is reconstructed using the charged tracks in the event constrained to the average position and effective spread of the e^+e^- collision point. For the b hadron reconstruction, charged tracks and electromagnetic calorimeter clusters with no associated track are combined into jets using a cone algorithm [23] with a cone half-angle of 0.65 rad and a minimum jet energy of 5.0 GeV [4]. The two most energetic jets of each event are assumed to contain the b hadrons and the energy and direction of each of the two b hadron candidates is reconstructed. In each hemisphere defined by the jet axis, a weight is assigned to each track and each cluster, where the weight corresponds to the probability that any one track or cluster is a product of the b hadron decay. The b hadron is reconstructed by summing the weighted momenta of the tracks and clusters. The reconstruction algorithm works for all b hadron species and is 100% efficient. Since this analysis aims at the reconstruction of $B_{\rm u,d}$ mesons which make up about 80% of the b hadron sample, b hadron candidates are referred to as B mesons in the following. Details of the reconstruction method are provided below.

[4] The cone jet finder provides the best b hadron energy and direction resolution compared to other jet finders.

4.2.1 Calculation of track weights

Two different types of weights are assigned to each charged track:

- $\omega_{\rm vtx}$, calculated from the impact parameter significances of the track with respect to both the primary and secondary vertices;
- $\omega_{\rm NN}$, the output of a neural network based on kinematics and track impact parameters with respect to the primary vertex.

The calculation of $\omega_{\rm vtx}$ requires the existence of a secondary vertex, whereas $\omega_{\rm NN}$ does not and is therefore available for all tracks.

Each jet is searched for secondary vertices using a vertexing algorithm similar to that described in [8], making use of the tracking information in both the $r-\phi$ and $r-z$ planes if available. If a secondary vertex is found, the primary vertex is re-fitted excluding the tracks assigned to the secondary vertex. Secondary vertex candidates are accepted and called 'good' secondary vertices if they contain at least three tracks and have a decay length > 0.2 mm. If a good secondary vertex is found, a weight is calculated for each track in the hemisphere of the jet using the impact parameter significance of the track with respect to both the primary and secondary vertices. This weight is given by

$$\omega_{\rm vtx} = \frac{R(b/\eta)}{R(b/\eta) + R(d/\sigma)} \, , \tag{1}$$

where b and η are the impact parameter and its error with respect to the secondary vertex, and d and σ are the same quantities with respect to the primary vertex. R is a symmetric function describing the impact parameter significance distribution with respect to a fitted vertex. The weight $\omega_{\rm vtx}$ shows a weak correlation with the momentum of the track.

For each track, the weight $\omega_{\rm NN}$ is calculated using an artificial neural network [24] trained to discriminate b hadron decay products from fragmentation tracks in a jet. The neural network was trained using as inputs the scaled track momentum $x_p = p/E_{\rm beam}$, the track rapidity relative to the estimated B direction, the impact parameters of the track with respect to the primary vertex in the $r-\phi$ and $r-z$ planes and the corresponding errors on the impact parameters [25]. As a preliminary estimate, the jet axis is taken as the estimated B direction. If a good secondary vertex exists, the track weight $\omega_{\rm NN}$ is combined with the vertex weight $\omega_{\rm vtx}$ using the prescription

$$\omega_{\rm tr} = \frac{\omega_{\rm NN} \cdot \omega_{\rm vtx}}{(1-\omega_{\rm NN}) \cdot (1-\omega_{\rm vtx}) + \omega_{\rm NN} \cdot \omega_{\rm vtx}} \, . \tag{2}$$

The weight $\omega_{\rm tr}$ in formula (2) comes close to a true probability and provides a separation power as good as the probability obtained from the combination of $\omega_{\rm NN}$ and $\omega_{\rm vtx}$ under the assumption that the two weights are uncorrelated and uniformly distributed. In the case where there is no good secondary vertex in the jet, the total track weight $\omega_{\rm tr}$ is simply given by $\omega_{\rm tr} = \omega_{\rm NN}$.

4.2.2 Calculation of cluster weights

Weights $\omega_{\rm ecl}$ and $\omega_{\rm hcl}$ are assigned to each electromagnetic and hadronic cluster, respectively. All electromagnetic and hadronic clusters in the hemisphere of the B are included in the calculation of the energy and direction of the B meson candidate. Clusters associated with a charged track have the estimated energy of the track subtracted. For each cluster, the rapidity with respect to the estimated B direction is calculated and then a weight assigned according to the b hadron decay product purity. The purity is obtained from a parameterisation of the corresponding Monte Carlo data as a function of the cluster energy.

4.2.3 Calculation of B direction

An interim estimate of the B momentum is obtained by a weighted sum of all tracks and clusters in the hemisphere:

$$\vec{p}_{\rm temp} = \sum_{i=1}^{N_{\rm track}} \omega_{{\rm tr},i} \cdot \vec{p}_i + \sum_{i=1}^{N_{\rm ecal}} \omega_{{\rm ecl},i} \cdot \vec{p}_i + \sum_{i=1}^{N_{\rm hcal}} \omega_{{\rm hcl},i} \cdot \vec{p}_i \qquad (3)$$

where $N_{\rm track}$, $N_{\rm ecal}$ and $N_{\rm hcal}$ denote the number of tracks, number of electromagnetic clusters and number of hadronic clusters, respectively. The rapidity calculation, for both tracks and clusters, is performed relative to an estimate of the B meson direction. The initial input for this axis is the jet direction calculated using tracks and unassociated electromagnetic clusters. Once the vector $\vec{p}_{\rm temp}$ has been calculated, an iterative procedure recalculates the weights with the rapidity calculated using the new B direction estimate.

If a good secondary vertex exists in a jet, the axis defined by the primary and secondary vertices yields additional direction information besides the B direction estimate obtained from the weighted momentum sum of tracks and clusters. To make optimal use of the two direction estimators available for a B candidate, the uncertainty of each direction estimator has to be calculated. The covariance matrices of the primary and secondary vertices determine the error on the B flight direction. The error on the momentum sum is estimated by removing each term in turn from the sum in equation (3), calculating the change in the B direction caused by this omission and adding up in quadrature the corresponding error contributions from each track and cluster. The final estimate of the B direction is obtained by taking the error-weighted sum of the B direction calculated with the momentum sum method and the B direction obtained from the primary and secondary vertex positions. The direction information in the $r-z$ plane of the secondary vertex is only used if the vertex is built with tracks that give rise to at least four hits in the z-layers of the silicon microvertex detector (the maximum number of these hits per track is two).

The error $\Delta\alpha$ on the weighted sum of both B direction estimators described in the previous paragraph is a measure for the quality of the B direction[5]. To improve the resolution on the B direction, which in turn dominates the Bπ mass resolution, a cut on $\Delta\alpha$ is imposed. Since this analysis aims at a separation of some of the $\rm B_J^*$ states by reconstructing different $\rm B_J^*$ decay channels rather than obtaining a very good Bπ mass resolution, the cut $\Delta\alpha < 0.035$ is rather loose. This cut removes the 20% of the B candidates with the poorest direction resolution, mainly those with no associated good secondary vertex.

4.2.4 Calculation of B energy

The B meson energy is calculated in analogy to the B momentum in equation (3), where $\vec{p}_i$ is replaced by $E_i = \sqrt{\vec{p}_i^{\,2} + m_i^2}$ with $m_i = m_{\pi^\pm}$ for tracks and $m_i = 0$ for clusters. The resolution on the total energy of the B candidate can be significantly improved by constraining the total centre-of-mass energy, $E_{\rm CM}$, to twice the LEP beam energy. Assuming a two-body decay of the $\rm Z^0$, we obtain:

$$E_{\rm B} = \frac{E_{\rm CM}^2 - M_{\rm recoil}^2 + M_{\rm B}^2}{2E_{\rm CM}} \ , \qquad (4)$$

[5]In the case where no good secondary vertex exists, $\Delta\alpha$ is simply given by the uncertainty on the momentum sum.

where the mass of the b hadron is set to the B meson mass $M_{\mathrm{B}} = 5.279$ GeV/c^2 and M_{recoil} denotes the mass recoiling against the B meson. The recoil mass and the recoil energy E_{recoil} are calculated by summing over all tracks and clusters[6] of the event weighted by $(1-\omega_i)$ and assuming the particle masses used in the calculation of E_i. To account for the amount of undetected energy mainly due to the presence of neutrinos, the recoil mass is scaled by the ratio of the expected energy in the recoil to the energy actually measured:

$$M_{\mathrm{recoil,new}} = M_{\mathrm{recoil,old}} \cdot \frac{E_{\mathrm{CM}} - E_{\mathrm{B}}}{E_{\mathrm{recoil}}} \tag{5}$$

where E_{B} is taken from equation (4). The new recoil mass value $M_{\mathrm{recoil,new}}$ obtained from equation (5) is substituted into equation (4) and the calculation of E_{B} is iterated. After two iterations the uncertainty on the B meson energy is minimised. To further improve the energy resolution, a minimum B energy of 15 GeV is required.

The distribution of the difference between the reconstructed and generated ϕ angle of simulated B mesons can be described by a fit to two Gaussians. The standard deviation of the narrower Gaussian is 14.2 mrad and 88% of the entries lie within 3σ. The corresponding quantities describing the θ resolution are $\sigma = 15.0$ mrad and 89%, respectively. The narrower Gaussian from a two Gaussian fit to the difference between the reconstructed and generated B meson energy has $\sigma = 2.3$ GeV, and 86% of the entries are contained within 3σ.

The complete B meson selection applied to the full data sample results in 574 288 tagged jets with a b purity of about 96%, as estimated from Monte Carlo. About 75% of the selected jets contain a good secondary vertex.

5 The decay $\mathrm{B}^* \to \mathrm{B}\gamma$

The photon produced in the decay $\mathrm{B}^* \to \mathrm{B}\gamma$ has an energy of about 46 MeV in the rest frame of the B^*. The mean energy of the photon in the laboratory frame is approximately 350 MeV, with a maximum energy below 800 MeV. Due to the kinematics of the process, these photons are produced predominantly in the core of the jet. A high particle density in this region gives rise to a high background level. Since a high B^* reconstruction efficiency is crucial for this analysis, photons are reconstructed in two ways: from energy deposits in the electromagnetic calorimeter and from converted photons in the tracking volume. The conversion probability within the OPAL tracking system for photons coming from the decay $\mathrm{B}^* \to \mathrm{B}\gamma$ is approximately 8%.

5.1 Reconstruction of photon conversions

The reconstruction of converted photons is optimised for the low energy region. The selection algorithm is partially based on quantities that have been used in earlier analyses [26] but tuned to obtain high efficiency rather than very good angular and momentum resolution. Given the low energy carried by these photons, we ignore calorimetry information and only use tracking information for the reconstruction of converted photons.

Tracks with a total momentum p below 1.0 GeV/c, opposite charge and a measured $\mathrm{d}E/\mathrm{d}x$ within three standard deviations of the expected value for electrons are combined into pairs. For each pair, the track with the greater scalar momentum is required to have a transverse

[6] Tracks and clusters not contained in the hemisphere of the B meson candidate have weights $\omega_i = 0$. ω_i denotes the weight $\omega_{\mathrm{tr},i}$, $\omega_{\mathrm{ecl},i}$ and $\omega_{\mathrm{hcl},i}$ for tracks, electromagnetic clusters and hadronic clusters, respectively.

momentum $p_t > 50$ MeV/c with respect to the beam axis and at least 20 hits out of a possible 159 per jet chamber sector. For the track with lower momentum a minimum p_t of 20 MeV/c is required. The asymmetric selection cuts for the two tracks in a pair guarantee at least one well measured track and reflect the fact that the electron and the positron of a converted photon tend to have different momenta in the laboratory frame. To suppress random track combinations, the distance of closest approach between the two tracks of a pair in the $r-\phi$ plane has to be smaller than 1.0 cm with an opening angle between the tracks at their point of closest approach smaller than 1.0 rad.

In order to make optimal use of all the available information, the following physical quantities of each conversion track pair candidate are fed into a neural network:

- the distance of closest approach between the two tracks in the $r-\phi$ plane;
- the radial distance with respect to the z axis of the first and last measured hit in the inner tracking chambers for each track;
- the radial distance with respect to the z axis of the common vertex[7] of both tracks obtained from a fit in the $r-\phi$ plane;
- the impact parameter with respect to the primary vertex in the $r-\phi$ plane of the reconstructed photon;
- the invariant mass of the track pair assuming both tracks to be electrons;
- the transverse momentum relative to the z axis of the lower momentum track.

All conversion candidates with a neural net output greater than 0.7 and a photon energy below 1.5 GeV are called 'good' conversion candidates for a given B meson candidate if the opening angle between the reconstructed B momentum vector and the reconstructed photon momentum vector is smaller than 90°. At this stage, an average of 0.82 good conversion candidates is selected per B candidate in both data and Monte Carlo. The candidate multiplicity distributions are shown in Figure 2a. The total efficiency to detect photons from the decay $B^* \to B\gamma$ with the conversion algorithm is estimated from simulation to be $(2.70 \pm 0.01_{\mathrm{stat}})\%$. The efficiency is rather independent of the photon energy from 1.0 GeV down to 200 MeV where it rapidly drops to zero due to track selection requirements. The amount of fake conversions in the selected sample is estimated from Monte Carlo simulation to be $(11.75 \pm 0.04_{\mathrm{stat}})\%$.

Fits to the difference between the reconstructed and generated photon energy in Monte Carlo are made using the sum of two Gaussians, both constrained to the same mean value. The narrower Gaussian has a standard deviation of 5 MeV at energies of 200 MeV up to 13 MeV at energies of 750 MeV and about 70% of the entries are contained within 3σ. Similar fits to the ϕ and θ resolutions give values of 3.4 mrad (70%) and 5.4 mrad (61%), respectively.

5.2 Reconstruction of photons in the electromagnetic calorimeter

Photons are also detected as showers in the barrel region of the electromagnetic calorimeter. The location and energy of these showers are obtained from a fit to the energy deposits in the individual lead glass blocks not associated with any charged track. The whole reconstruction

[7] The z position of this vertex is fitted independently and the reconstructed photon vector is constrained to the z coordinate of the primary vertex to improve the accuracy of the θ determination.

method has been shown to work in the dense environment of hadronic jets down to photon energies as low as 150 MeV. The details of the reconstruction are described in [27].

Showers in the electromagnetic calorimeter are accepted as photon candidates if they have an energy in the range 200 MeV to 850 MeV and a photon probability $P_\gamma > 0.20$, where P_γ is the output of a simplified neural network [27]. If the opening angle between such a shower and a reconstructed B candidate is less than 90°, this shower is considered a 'good' photon candidate for the corresponding B candidate. On average, there are 4.59 (4.38) good calorimeter photon candidates per B candidate selected in the data (Monte Carlo) sample. To correct for the observed discrepancy, the Monte Carlo is reweighted to the data distribution shown in Figure 2b. The efficiency to detect a photon from the decay $B^* \to B\gamma$ in the electromagnetic calorimeter is estimated to be $(14.52 \pm 0.03_{\rm stat})\%$ using Monte Carlo simulated events. The fraction of fake photons arising from charged tracks and neutral hadrons in the sample ranges from 32% at photon energies of 850 MeV up to 43% at photon energies of 200 MeV. If compared with the selected conversion sample, the selection of $B^* \to B\gamma$ photons in the electromagnetic calorimeter has a much higher efficiency but lower purity.

As with the converted photons, the energy resolution has been determined from Monte Carlo simulation using a double Gaussian fit. The narrower Gaussian has a width of 20 MeV at photon energies of 250 MeV and increases up to 86 MeV at energies of 800 MeV, and about 75% of the entries are contained within 3σ. Similar fits to the ϕ and θ resolutions give values of 3.6 mrad (65%) and 3.6 mrad (72%), respectively. In contrast to the conversion sample, photons reconstructed in the electromagnetic calorimeter have much higher energy uncertainties, but the θ resolution in particular is better.

5.3 Reconstruction of $B^* \to B\gamma$ decays

Each reconstructed B meson candidate is combined with all good conversion and calorimeter candidates to reconstruct B^* candidates. The invariant mass of a $B\gamma$ combination is defined as

$$M_{B\gamma} = \sqrt{M_B^2 + 2E_B E_\gamma - 2p_B 2p_\gamma \cos\alpha} \quad , \tag{6}$$

where M_B is 5.279 GeV/c^2 and α is the measured angle between the B meson and the photon candidate. The mass difference $\Delta M = M_{B\gamma} - M_B$ between the B^* candidate and the B is calculated by simply subtracting the nominal B mass of $M_B = 5.279$ GeV/c^2 from $M_{B\gamma}$.

The mass difference distributions of the conversion sample observed in the data and the corresponding Monte Carlo background are shown in Figure 3a. The background is normalised to the data in the sideband region 0.09 GeV/c^2 $< \Delta M <$ 0.20 GeV/c^2. The background subtracted signal of Figure 3b is fitted to the sum of two Gaussians fixed to the same mean, where one of the Gaussians is allowed to have asymmetric width. The observed asymmetry of the mass resolution of the conversion sample is well simulated in the Monte Carlo and is due to the very loose track requirements of the lower momentum track of the conversion pair. A mass difference of $\Delta M = (45.87 \pm 0.25_{\rm stat})$ MeV/c^2 is obtained from the fit to the data, where the error is statistical only. This result agrees well with the current world average value of (45.78 ± 0.35) MeV/c^2 [2].

The ΔM distribution using calorimeter photons is shown in Figure 4a. The background is taken from Monte Carlo simulation and normalised to the data in the sideband region 0.10 GeV/c^2 $< \Delta M <$ 0.20 GeV/c^2. The same fit function as for the photon conversion sample is used to obtain the mass difference ΔM from the background subtracted signal distribution

in Figure 4b. A value of $(47.30 \pm 0.61_{\mathrm{stat}})$ MeV/c^2 is obtained from this fit, which is consistent within two sigma with the result from the fit to the conversion signal.

For the B* sample reconstructed with photon conversions, the mass resolution is dominated by the uncertainty on the reconstructed B direction. For the calorimeter photon sample, the B* mass resolution suffers in addition from the energy resolution of the calorimeter. Due to the high background of fake photons and the moderate energy resolution at low photon energies, the signal-to-background ratio is rather poor for calorimeter photons. Therefore, uncertainties in the B* reconstruction using these photons are dominated by systematic errors on the background shape and energy calibration. All systematic uncertainties arising from the B* reconstruction will be discussed in Section 8.

5.4 The B* probability $\mathcal{W}$(B*)

To select samples enhanced and depleted in B* mesons, a B* probability is assigned to each B candidate. This probability combines information from both conversion and calorimeter photon candidates and represents the probability that a B candidate is the true daughter of a B* meson. Only the best conversion and best calorimeter candidate assigned to any one B candidate are considered in the calculation of this probability, where the best candidate is defined as that which gives $\Delta M = M_{\mathrm{B}\gamma} - M_{\mathrm{B}}$ closest to the measured value of 45.78 MeV/c^2 [2].

This weight is constructed by parametrising the purity of the mass difference distribution in several variables in Monte Carlo data. For calorimeter photon candidates, this parametrisation is performed as a function of the photon probability, P_γ (see Subsection 5.2), and the total number of good calorimeter candidates found per B candidate. For each B candidate, a single weight is calculated by taking the simple mean of the weight resulting from each of the above parametrisations.

Similarly, for conversion photon candidates, the parametrisation is performed in ΔM as a function of the total number of conversion candidates, and a weight is extracted as for the calorimeter candidates. The two weights obtained from conversion and calorimeter photons are combined by taking their mean.

The resulting weight $\mathcal{W}$(B*) is shown in Figure 5a for Monte Carlo and data, and the relative contributions from jets containing a B* and jets containing no B* as seen in the simulation are shown. The primary features of the $\mathcal{W}$(B*) distribution are:

- a peak at $\mathcal{W}(\mathrm{B}^*) = 0.625$, corresponding to B candidates with no associated good conversion or calorimeter photon candidate;
- a peak at $\mathcal{W}(\mathrm{B}^*) = 0.632$, containing B candidates with no good conversion candidate and a best calorimeter candidate having a Bγ mass far away from the nominal B* mass;
- a peak around $\mathcal{W}(\mathrm{B}^*) = 0.656$, containing B candidates with the best calorimeter candidate close to the nominal B* mass;
- a peak at $\mathcal{W}(\mathrm{B}^*) = 0.715$, containing B candidates with the best calorimeter candidate being close to the nominal B* mass and having a high photon probability P_γ;
- the tail towards high B* probabilities is made up by best conversion candidates very close to the nominal B* mass.

The assignment of the specific photon candidate samples to the peaks and to the tail of the $\mathcal{W}$(B*) distribution is based on Monte Carlo information. Figure 5b shows the ratio ε(B*)/ε(B)

versus $\mathcal{W}(\mathrm{B}^*)$. $\varepsilon(\mathrm{B}^*)$ refers to the efficiency to select a B meson from a true $\mathrm{B}^* \to \mathrm{B}\gamma$ decay and $\varepsilon(\mathrm{B})$ is the efficiency to select a B meson which has not come from a B^*. In general, the Monte Carlo simulation of $\mathcal{W}(\mathrm{B}^*)$ describes the data adequately. A comparison of the Monte Carlo and data distributions yields a χ^2 per degree of freedom of 2. A cut on $\mathcal{W}(\mathrm{B}^*)$ allows to produce samples of B candidates with different B^* fractions. Further details and systematic studies concerning $\mathcal{W}(\mathrm{B}^*)$ are given in Section 8.

6 Reconstruction of orbitally-excited B mesons

All B_J^* candidates, even those expected to decay into $\mathrm{B}^*\pi^\pm$, are reconstructed using the measured 4-momenta of the B meson and the pion. B candidates are selected and reconstructed as described in Section 4 and combined with charged pion candidates. Pions produced in the decay of a B_J^* will be referred to as 'signal pions'. Since the B_J^* decays strongly, signal pions are expected to be associated to the primary event vertex rather than to a possible secondary vertex. In comparison with other pions created in the fragmentation process, signal pions are expected to have a large longitudinal momentum p_l with respect to the jet axis. These are the basic characteristics used to separate signal pions from B decay products and from fragmentation tracks. A significant number of non-resonant fragmentation pions are expected to be produced near a B meson. The kinematics of these pions is similar to the signal pions, giving rise to a combinatorial background in the invariant mass of $\mathrm{B}\pi$ candidates. This background is further enhanced by the inability to unambiguously associate all B decay tracks with the secondary vertex.

6.1 Pion selection

The signal pion selection for this analysis makes use of techniques used in [8] and [11]. All charged tracks that are well measured according to a standard track selection [28] are considered as possible signal pion candidates if they belong to the same jet as the B candidate. Additionally, the following selection cuts are applied in the given order:

- The measured ionisation energy loss $\mathrm{d}E/\mathrm{d}x$ has to be consistent with the expected value for pions within 2.6 standard deviations, if $\mathrm{d}E/\mathrm{d}x$ information is available for this track.
- To suppress B decay tracks, the track weight ω_{NN} as described in Subsection 4.2 has to be smaller than 0.9.
- The B decay track rejection is improved by the requirement $\omega_{\mathrm{NN2}} < 0.7$, where ω_{NN2} is a neural net output defined for jets containing a secondary vertex. The inputs for ω_{NN2} are similar to the inputs for ω_{NN}, but also the impact parameter significances in the $x-y$ and the z plane with respect to the secondary vertex are used.
- From all tracks that pass the previous selection criteria, only the one with the highest longitudinal momentum with respect to the jet axis, $p_l^{\max}$, is kept for each B candidate,
- A reduction of B decay track background in the $p_l^{\max}$ sample is obtained by the requirements $\omega_{\mathrm{NN}} < 0.80$ and $\omega_{\mathrm{NN2}} < 0.50$ [8].

[8] If no secondary vertex is present in the jet, the cut $\omega_{\mathrm{NN}} < 0.50$ instead of $\omega_{\mathrm{NN2}} < 0.50$ is applied.

- Fragmentation tracks in the $p_l^{\max}$ sample are removed with the requirement $\omega_{\rm NN} > 0.20$. Since $\omega_{\rm NN}$ is designed to achieve optimal separation of b hadron decay tracks from fragmentation tracks using tracking information *and* kinematics, the Monte Carlo indicates a fairly flat $\omega_{\rm NN}$ distribution for signal pions. On the contrary, fragmentation tracks peak at zero.

- A momentum of $p > 1.0$ GeV/c is required for signal pion candidates. In the simulation, the momentum distribution of signal pions has a mean value of 2.9 GeV/c with an RMS of 1.3 GeV/c before the cut is applied. The $\rm B_J^*$ mass spectrum for single pion transitions is not influenced by the momentum requirement.

6.2 $\rm B\pi^{\pm}$ mass spectrum

The signal pion candidate passing the selection cuts described in subsection 6.1 is combined with the corresponding B candidate to form a $\rm B_J^*$ candidate. The invariant mass is calculated using equation (6) as for the $\rm B^*$ mass, where the photon is replaced by a pion and the appropriate pion mass term is added. The cuts of the signal pion selection have been chosen to obtain an acceptable signal-to-background ratio at high signal efficiency. The order of the non-commuting selection requirements using $\omega_{\rm NN}$, $\omega_{\rm NN2}$ and $p_l^{\max}$ aims to maximise the difference between the shape of the signal and background contributions to the $M_{\rm B\pi}$ distribution.

Due to the intrinsic widths of the $\rm B_J^*$ states and the limited detector resolution, only a single peak is seen in the $M_{\rm B\pi}$ spectrum of Figure 6a on top of the combinatorial background. According to the simulation, the $M_{\rm B\pi}$ resolution can be described by the sum of a narrow Gaussian and an asymmetric Gaussian both constrained to the same mean value (see Figure 7). The mass resolution depends linearly on $M_{\rm B\pi}$. In the $\rm B_J^*$ signal region around 5.7 GeV/c^2 the standard deviation of the narrow Gaussian is $\sigma = 33$ MeV/c^2, and 85% of the resolution function entries are contained within 3σ. The Monte Carlo combinatorial background is checked against data using different test samples strongly enhanced in each of the following physics background sources: 1. fake $\rm B_J^*$ candidates from light and charm quark events; 2. fake $\rm B_J^*$ arising from true b hadrons combined with a pion from the weak decay of the b hadron itself; 3. fake $\rm B_J^*$ formed by combining true b hadrons with fragmentation tracks which have not come from a $\rm B_J^*$ resonance. The simulation indicates that each test sample is strongly enhanced in the background source under study and that the $\rm B_J^*$ signal is suppressed by about a factor of eight compared to the original $\rm B_J^*$ signal selection. The $\rm B\pi$ mass distributions of the data background samples are compared with the corresponding Monte Carlo mass distributions (see also Subsection 8.2). In the case of a significant deviation, the simulated background is reweighted to the data. The Monte Carlo background distribution so obtained is fitted using a threshold function of the form $C_1 \cdot \sqrt{x - (m_{\rm B} + m_\pi)} \cdot (\Phi(\frac{x - C_2}{C_3}))^{C_4}$, where Φ is the Landau density function[9]. This background function gives a good empirical fit with only four free parameters C_i. The fitted Monte Carlo background is normalised in the sideband region 6.04 GeV/c^2 $< M_{\rm B\pi} <$ 7.04 GeV/c^2 and subtracted from the data distribution. The obtained $\rm B_J^*$ signal is shown in Figure 6b. The reconstruction efficiency for $\rm B_J^*$ depends on the reconstructed mass $M_{\rm B\pi}$. Monte Carlo studies indicate that the efficiency becomes smaller as $M_{\rm B\pi}$ decreases, mainly due to the $p_l^{\max}$ requirement. The $\rm B_J^*$ distribution of Figure 6b is corrected for efficiency and the resulting signal is shown in Figure 6c.

[9] $\Phi(\lambda) = \frac{1}{2\pi i} \int_{c-i\infty}^{c+i\infty} e^{\lambda s + \ln s} ds$

The mean mass, shape and yield of the observed B_J^* signal is in agreement with other measurements [8–11]. The structure of the $B\pi^\pm$ mass spectrum is too broad to stem from a single narrow resonance and leaves room for interpretation. The peak is expected to contain two broad and two narrow B_J^* states and due to the photon which is not taken into account in the case of the decay $B_J^* \to B^*\pi$, part of the true mass spectrum is shifted to lower mass by 46 MeV/c^2. The fraction of B_{sJ}^* decays in the peak due to the misidentification of kaons is smaller than 4% assuming the B_{sJ}^* production rate measured in [8]. In addition, the peak may contain contributions from $B_J^* \to B^{(*)}\pi\pi$ giving rise to satellite peaks in the region 5.4 GeV/c^2 < $M_{B\pi}$ < 5.6 GeV/c^2, since the second pion is not included in the invariant mass calculation. If broad B_J^* states have masses close to the $B\pi$ threshold, they can have an asymmetric signal shape due to phase space suppression. Also contributions from radially-excited B mesons in the decay channels $B^{(*)\prime} \to B^{(*)}\pi$ and $B^{(*)\prime} \to B^{(*)}\pi\pi$ may contribute, although the production rate of $B^{(*)\prime}$ is assumed to be small compared to the B_J^* production rate according to [29]. Since there are several ambiguities, e.g. due to $B_J^* \to B^{(*)}\pi\pi$, $B^{(*)\prime}$ decays and uncertainties in the combinatorial background, further details of the signal composition can only be obtained by making additional, model dependent assumptions.

Systematic errors arising from the signal pion selection, especially the uncertainties assigned to the combinatorial background in the $B\pi^\pm$ mass spectrum, will be discussed in detail in Section 8.

7 Results

The branching ratio of orbitally-excited B mesons decaying into $B^*\pi$ is obtained using the sample of reconstructed B_J^* candidates and the $\mathcal{W}(B^*)$ distribution. As the weight $\mathcal{W}(B^*)$ is calculated for each B meson candidate, it is available for each B_J^* candidate. A cut is applied on $\mathcal{W}(B^*)$ to divide the total B_J^* sample into a sample of B_J^* candidates enriched in the decay $B_J^* \to B^*\pi^\pm$ and a sample of B_J^* candidates depleted in the decay $B_J^* \to B^*\pi^\pm$. The statistical error on $BR(B_J^* \to B^*\pi)$ is minimal if both subsamples are of the same size. Systematic uncertainties in the $B\pi^\pm$ background have minimal impact on $BR(B_J^* \to B^*\pi)$ if the signal-to-background ratio is the same for the $B\pi^\pm$ mass distributions of the B^*-enriched and the B^*-depleted sample. The optimal cut on $\mathcal{W}(B^*)$ is 0.648, fulfilling the minimal systematic error requirement and coming as close as possible to the minimum statistical error requirement (see Figure 5).

The B^* enrichment and depletion method can be evaluated by the different selection efficiencies for the transitions $B_J^* \to B^*\pi^\pm$ and $B_J^* \to B\pi^\pm$ in the B^*-enriched and B^*-depleted samples. With the definitions

- $\varepsilon_{\rm E}^*$: $B_J^* \to B^*\pi$ efficiency of B^*-enriched sample;
- $\varepsilon_{\rm D}^*$: $B_J^* \to B^*\pi$ efficiency of B^*-depleted sample;
- $\varepsilon_{\rm E}$: $B_J^* \to B\pi$ efficiency of B^*-enriched sample;
- $\varepsilon_{\rm D}$: $B_J^* \to B\pi$ efficiency of B^*-depleted sample;
- efficiency ratios: $e_0 = \varepsilon_{\rm D}/\varepsilon_{\rm E}^*$; $e = \varepsilon_{\rm E}/\varepsilon_{\rm D}$; $e^* = \varepsilon_{\rm D}^*/\varepsilon_{\rm E}^*$,

we calculate from Monte Carlo the efficiency values presented in Table 2. The numbers reflect the cut on $\mathcal{W}(B^*)$ and thus the quality of the B^* enrichment versus the B^* depletion. Only

the efficiency ratios given in the right column of Table 2 but not the absolute efficiencies are needed for the determination of $\mathrm{BR}(\mathrm{B}_J^* \to \mathrm{B}^*\pi)$. For the $\mathrm{BR}(\mathrm{B}_J^* \to \mathrm{B}^*\pi)$ measurement, the

efficiency		efficiency ratio	
$\varepsilon_{\mathrm{E}}^*$	0.05084 ± 0.00023	e_0	1.566 ± 0.010
$\varepsilon_{\mathrm{D}}^*$	0.06680 ± 0.00026	e	0.578 ± 0.005
ε_{E}	0.04601 ± 0.00030	e^*	1.314 ± 0.008
ε_{D}	0.07962 ± 0.00039		

Table 2: Efficiencies for the reconstruction of B_J^* decaying to $\mathrm{B}^*\pi$ and to $\mathrm{B}\pi$. The numbers are calculated with respect to the total number of B_J^* passing the B selection in the Monte Carlo. Therefore, the numbers reflect the effect of the cut on $\mathcal{W}(\mathrm{B}^*)$ and the charged pion selection. Also a factor of 2/3 assuming isospin symmetry to account for decays of B_J^* via neutral pions is included in each of the efficiency values. The errors are statistical errors only.

invariant $\mathrm{B}\pi^\pm$ mass distributions of the B^*-enriched and the B^*-depleted sample are used. Both mass distributions are independent subsamples of the distribution shown in Figure 6, but contain different compositions of $\mathrm{B}_J^* \to \mathrm{B}^*\pi^\pm$ and $\mathrm{B}_J^* \to \mathrm{B}\pi^\pm$ decays. Figures 8 and 9 show the $\mathrm{B}\pi^\pm$ mass distributions for the B^*-enriched and the B^*-depleted sample, respectively. The Monte Carlo background distributions of both samples are corrected using a procedure explained in Sections 6 and 8 and the same fit as for the background of the total B_J^* sample (see Section 6) is performed. The fitted background functions are normalised in the sideband region $6.04\ \mathrm{GeV}/c^2 < M_{\mathrm{B}\pi} < 7.04\ \mathrm{GeV}/c^2$ and subtracted from the corresponding data distributions. From the resulting signal peaks of Figures 8b and 9b, $\mathrm{BR}(\mathrm{B}_J^* \to \mathrm{B}^*\pi)$ is obtained. With the efficiency ratios defined as above, we deduce the following formula:

$$\mathrm{BR}(\mathrm{B}_J^* \to \mathrm{B}^*\pi) = e_0 \cdot \frac{N_{\mathrm{E}} - e \cdot N_{\mathrm{D}}}{(e_0 - e^*) \cdot N_{\mathrm{E}} + (1 - e \cdot e_0) \cdot N_{\mathrm{D}}} \quad , \tag{7}$$

where N_{E} (N_{D}) denotes the number of B_J^* signal entries of the B^*-enriched (B^*-depleted) sample. In the data, $N_{\mathrm{E}} = (8782 \pm 252_{\mathrm{stat}})$ and $N_{\mathrm{D}} = (12051 \pm 295_{\mathrm{stat}})$ B_J^* candidates are observed in the $M_{\mathrm{B}\pi}$ signal window $(5.3 - 6.1)\ \mathrm{GeV}/c^2$. Using the numbers for the efficiency ratios e_0, e and e^* presented in Table 2, we calculate $\mathrm{BR}(\mathrm{B}_J^* \to \mathrm{B}^*\pi) = 0.85$.

The statistical errors on N_{E} and N_{D} result in a total error on the branching ratio of ± 0.13. Besides this error, statistical uncertainties due to the sideband normalisation have been taken into account. Since the samples are mutually exclusive, the statistical errors of the sideband normalisation of both samples are independent. The contributions of the B^*-enriched and the B^*-depleted sample sideband normalisation to the statistical error on $\mathrm{BR}(\mathrm{B}_J^* \to \mathrm{B}^*\pi)$ are $^{+0.17}_{-0.18}$ and ± 0.15, respectively. Adding all quoted errors in quadrature, the branching ratio of orbitally-excited B mesons decaying into B^* is measured to be

$$\mathrm{BR}(\mathrm{B}_J^* \to \mathrm{B}^*\pi) = 0.85\,^{+0.26}_{-0.27}\,,$$

where the error is the statistical error only. This result may also include small contributions from $\mathrm{B}_J^* \to \mathrm{B}^*\pi\pi$ and $\mathrm{B}_J^* \to \mathrm{B}\pi\pi$ transitions.

We further investigate the composition of the reconstructed B_J^* sample according to the decays $\mathrm{B}_J^* \to \mathrm{B}^*\pi^\pm$ and $\mathrm{B}_J^* \to \mathrm{B}\pi^\pm$. By subtracting from the $\mathrm{B}\pi$ mass distribution of the B^*-enriched sample the corresponding distribution of the B^*-depleted sample multiplied by a scale

factor, a $B\pi^{\pm}$ mass distribution containing $B^*_J \to B^*\pi^{\pm}$ transitions only is obtained. The scale factor is the ratio of the $B^*_J \to B\pi^{\pm}$ efficiencies of both samples, $e = \varepsilon_{\rm E}/\varepsilon_{\rm D}$. In a similar way, a mass distribution with $B^*_J \to B^*\pi^{\pm}$ decays subtracted off is obtained. The corresponding efficiency-corrected $B\pi^{\pm}$ mass distributions for pure $B^*_J \to B^*\pi^{\pm}$ and pure $B^*_J \to B\pi^{\pm}$ transitions are shown in Figure 10.

A significant excess of entries is seen in the pure $B^*_J \to B^*\pi^{\pm}$ distribution at masses around 5.7 GeV/c^2 with tails down to 5.5 GeV/c^2 and up to 6.0 GeV/c^2. The narrow peak in the $B^*_J \to B^*\pi^{\pm}$ distribution is most likely due to $B_1(3/2) \to B^*\pi^{\pm}$ and $B^*_2 \to B^*\pi^{\pm}$ decays. To obtain the true mass values of the $B^*\pi$ states, the entries have to be shifted to higher masses by 46 MeV/c^2.

In the pure $B^*_J \to B\pi^{\pm}$ mass distribution, a small excess is observed in the region up to 5.85 GeV/c^2. This excess can be assigned to the decays $B^*_2 \to B\pi^{\pm}$ and $B^*_0 \to B\pi^{\pm}$. Since the statistical significance of the excess in the $B^*_J \to B\pi^{\pm}$ mass distribution is small, no further conclusion is drawn from Figure 10b.

8 Systematic uncertainties

The main sources of systematic error on $BR(B^*_J \to B^*\pi)$ are uncertainties in the efficiency ratios, uncertainties in the modelling of the combinatorial $B\pi^{\pm}$ background and systematic errors on the sideband normalisation of the B^*-enriched and B^*-depleted samples. Each contribution to the total error on $BR(B^*_J \to B^*\pi)$ is listed in Table 3 and discussed in the following subsections.

8.1 Reconstruction efficiency

For the determination of $BR(B^*_J \to B^*\pi)$, the Monte Carlo simulation is used to calculate the efficiency ratios e, e^* and e_0. The systematic errors on these ratios are dominated by uncertainties in the photon reconstruction. The simulation is checked against data using known properties of B^* and π^0. The latter are formed by a pairwise combination of two good conversion candidates or one good conversion and one good calorimeter candidate assigned to the same B candidate.

- In both the calorimeter and conversion samples the positions of both the B^* signal peak and the π^0 peak in the data are duplicated within the statistical errors by the Monte Carlo simulation. The simulated shape of the peaks agrees well with the shape observed in data. The contribution to the branching fraction measurement arising from statistical uncertainties on the fits to the B^* signal peak, and on the difference between the reconstructed and generated B^* mass in the simulation are quantified by adjusting the mass to the current world average [2] and systematically shifting it to higher and lower values. For the conversion sample, a shift of ± 1.0 MeV/c^2 in the B^* peak position is made, but since the cut on $\mathcal{W}(B^*)$ is such that all conversion candidates with a $M_{B\gamma}$ mass in the M_{B^*} region are selected, the resulting effect on $BR(B^*_J \to B^*\pi)$ is negligible. For the calorimeter photon sample a shift of ± 2.0 MeV/c^2 in the B^* peak position is made, resulting in a variation of $BR(B^*_J \to B^*\pi)$ by $^{+0.007}_{-0.005}$.

- The number of B^* and π^0 candidates found in the corresponding mass peaks of the conversion sample has been compared with the corresponding results from the Monte

Carlo simulation. The observed yields agree within the statistical error of 5%. The production rates of B^* and π^0 have been measured with a relative precision of 5.3% and 2.9% [2], respectively, and the corresponding JETSET rates are in agreement with these measurements. To account for the quoted uncertainties, the calculation of efficiency ratios is repeated on Monte Carlo with the reconstruction efficiency of conversion photons in the decay $B^* \to B\gamma$ changed by $\pm 10\%$, resulting in a total error on $BR(B_J^* \to B^*\pi)$ of $^{+0.019}_{-0.018}$.

After the subtraction of the Monte Carlo background, the yield of B^* candidates in the calorimeter sample is greater in data than in the Monte Carlo sample. The Monte Carlo background is underestimated in the B^* signal region or the efficiency for calorimeter photons from B^* is underestimated. Since the source of the discrepancy cannot be assigned unambiguously, the Monte Carlo efficiency for calorimeter photons of the decay $B^* \to B\gamma$ is varied by a factor of 0.9 to 1.15, the lower value being consistent with the corresponding uncertainty assigned in the conversion sample and the factor 1.15 covering the observed B^* yield in data. The change in $BR(B_J^* \to B^*\pi)$ corresponding to this variation is $^{+0.036}_{-0.047}$.

- The number of good calorimeter photon candidates (Figure 2b) is not modelled well in the simulation. Therefore, the Monte Carlo distribution is reweighted to the corresponding data distribution. The reweighting clearly improves the general agreement between data and Monte Carlo and has an impact on the efficiency rations e, e^* and e_0. The central value of $BR(B_J^* \to B^*\pi)$ changes by -0.059 due to the reweighting. To quantify the uncertainty in the reweighting procedure we take half of the total change of the central value as the error on $BR(B_J^* \to B^*\pi)$.

- In a B_J^* decay, the helicity angle θ^* is the angle between the signal pion momentum measured in the B_J^* rest frame and the momentum of the B_J^* in the lab frame. The B_0^* and the $B_1(1/2)$ can only decay via S-wave transitions and therefore the corresponding distributions of helicity angle are flat. The angular distributions of the ($B_1(3/2)$, B_2^*) doublet have not yet been measured. Thus each of the B_J^* states has been generated with a flat $\cos\theta^*$ distribution in the simulation. As the signal pion selection acceptance depends on $\cos\theta^*$, the different B_J^* efficiencies $\varepsilon_i^{(*)}$ are sensitive to the shape of $\cos\theta^*$. According to [30] the $B_1(3/2)$ and the B_2^* are expected to have the same $\cos\theta^*$ distribution for any initial b polarisation:

$$\frac{1}{\Gamma}\frac{d\Gamma}{d\cos\theta^*}(B_1(3/2), B_2^* \to B, B^*\pi) = \frac{1}{4}\left(1 + 3\cos^2\theta^* - 6w_{3/2}(\cos^2\theta^* - \frac{1}{3})\right) \qquad (8)$$

where $w_{3/2}$ is the probability that fragmentation leads to a state with the maximum helicity value of 3/2 for the light degrees of freedom. The value of $w_{3/2}$ is not predicted by theory. Therefore, the Monte Carlo $\cos\theta^*$ distributions of $B_1(3/2)$ and B_2^* have been reweighted to cover the whole range $w_{3/2} = 0 - 1$. The corresponding total change in $BR(B_J^* \to B^*\pi)$ is $^{+0.040}_{-0.034}$.

- The mass dependent efficiency correction of the B_J^* signal of both the B^*-enriched and B^*-depleted samples produces a deviation in $BR(B_J^* \to B^*\pi)$. To account for any mis-modelling in the simulated mass dependence of the efficiency, half of this deviation is taken as the systematic error: ± 0.018.

- The limited Monte Carlo statistics give rise to uncertainties in the calculated efficiency ratios. This causes an additional error on $BR(B_J^* \to B^*\pi)$ of ± 0.018.

Source	range	$\Delta(\mathrm{BR}(\mathrm{B}_J^* \to \mathrm{B}^*\pi))$
B^* efficiency ($\gamma \to \mathrm{e}^+\mathrm{e}^-$) variation	[0.90, 1.10]	+0.019 −0.018
reconstructed B^* mass (ECAL)	± 2 MeV/c^2	+0.007 −0.005
B^* efficiency (ECAL) variation	[0.90, 1.15]	+0.036 −0.047
reweighting of $N_{\gamma_{\mathrm{ECAL}}}$	stat. error	± 0.030
statistical error on efficiency ratios	$\approx 1\%$	± 0.018
$\cos\theta^*$ dependency	$w_{3/2} \in [0, 1]$	+0.040 −0.034
$M_{\mathrm{B}\pi}$ dependence of B_J^* efficiency		± 0.018
udsc tracks background modelling	corr. on/off	± 0.002
B decay tracks background modelling	corr. on/off	± 0.017
b fragmentation tracks background modelling	corr. on/off	± 0.005
relative composition of background sources	$\pm 20\%$	+0.027 −0.037
variation of signal π selection cuts		+0.042 −0.048
variation of cuts on $\mathcal{W}(\mathrm{B}^*)$		+0.030 −0.043
B_{sJ}^* reflections		+0.006 −0.026
$\mathrm{B}^{(*)\prime}$ reflections		+0.000 −0.017
track parameter resolution variation	$\pm 10\%$	< 0.010
sideband range variation	± 100 MeV/c^2	+0.076 −0.057
Total		+0.12 −0.12

Table 3: Systematic errors of the $\mathrm{BR}(\mathrm{B}_J^* \to \mathrm{B}^*\pi)$ measurement. Detailed information for each uncertainty is given in the text, as well as a discussion of uncertainties which are negligible and thus excluded from this table.

8.2 Combinatorial $\mathrm{B}\pi^\pm$ background

Uncertainties in the shape of the simulated background have an impact on the number of signal candidates N_{E} and N_{D}. Since the combinatorial backgrounds in both the B^*-enriched and the B^*-depleted samples are affected by systematic shifts in a similar way, the analysis is expected to be rather robust against possible uncertainties in the Monte Carlo background simulation. The cut value for $\mathcal{W}(\mathrm{B}^*)$ is chosen to minimise the resulting error on $\mathrm{BR}(\mathrm{B}_J^* \to \mathrm{B}^*\pi)$ (see Section 7).

- Data test samples are developed in which individual background sources are substantially enhanced, to allow detailed studies of the $\mathrm{B}\pi^\pm$ combinatorial background. The background is divided into three different classes: tracks combined with mistagged B candidates in light and charm quark events (udsc flavour), b hadron decay tracks combined with true b hadrons (b hadron decay) and b fragmentation tracks combined with true b hadrons (b fragmentation). Since the quality of the Monte Carlo background modelling may be different for different kinematical regions, the selection criteria of each test sample are chosen to cover a substantial fraction of the kinematical region of the signal pion selection. Furthermore, a purity of at least 90% for the background source under study and a B_J^* signal fraction smaller than 1.5% is demanded. These requirements are achieved by inverting cuts of the original B_J^* selection. For each test sample, the $\mathrm{B}\pi^\pm$ invariant mass distribution observed in data is compared with the corresponding Monte Carlo distribution normalised to the same number of selected B candidates. The mass distributions and their bin-by-bin ratios data/Monte Carlo are shown in Figure 11. The different ratios are fitted with simple polynomials. The latter are used to correct the

shape of the original Monte Carlo $B\pi^{\pm}$ mass distributions for each background source separately. The systematic uncertainty on each background source is given by the difference between the corrected and the uncorrected shape of the $B\pi^{\pm}$ mass distribution. This results in systematic errors on $BR(B_J^* \to B^*\pi)$ of ± 0.002, ± 0.017 and ± 0.005, for the light and charm background, the b hadron decay background and the b fragmentation background, respectively.

All test samples and background corrections described are obtained using the full B_J^* sample but applied to the background distributions of the B^*-enriched and B^*-depleted sample, since it is assumed that the B^* selection does not affect a possible mismodelling of the Monte Carlo $B\pi^{\pm}$ background.

Since the light and charm quark sample described above does not have the same charm quark content as the non-b background of the B_J^* signal selection, an additional cross check is performed. Charm events are tagged using reconstructed D^{*+} candidates in five different decay channels, as described in [31]. This results in a sample with the same composition of light flavour and charm flavour as in the B_J^* signal selection and less than 10% b flavour. The observed Monte Carlo deviation in the $B\pi^{\pm}$ mass spectrum of this D^{*+} sample is consistent with the deviation seen in the first test sample. Due to the low statistics of the D^{*+} sample only the sample described first is used.

- The composition of the $B\pi^{\pm}$ background, as seen in Monte Carlo after the corrections have been applied, is varied for each source. The fraction of each of the three background sources described earlier is varied by $\pm 20\%$. This results in an additional systematic error on $BR(B_J^* \to B^*\pi)$ of $^{+0.027}_{-0.037}$.

- The Peterson fragmentation parameter ϵ_b has been varied in the range $0.0028 - 0.0057$ to cover uncertainties in the average fraction of the beam energy carried by the weakly decaying b hadron, $\langle x_E \rangle$, and in the shape of the fragmentation function. This variation causes a small change in the $B\pi^{\pm}$ background shape. The effect on $BR(B_J^* \to B^*\pi)$ is smaller than 0.002.

- The charged particle multiplicity of weakly decaying b hadrons is considered as a source of systematic uncertainty on the $B\pi^{\pm}$ background. The average charged multiplicity including K^0 and Λ decay products is varied in the range $5.375 - 5.865$ in the simulation (see [32]). The observed effect on the $B\pi^{\pm}$ background shape results in an error on $BR(B_J^* \to B^*\pi)$ smaller than 0.002.

8.3 Other sources of systematic uncertainties and consistency checks

The following systematic studies have been performed in addition to the studies described in Subsections 8.1 and 8.2.

- The range of the sideband used for the background normalisation is varied by ± 100 MeV on each side for both the B^*-enriched and B^*-depleted sample. The quadratic sum of the differences observed in the number of signal entries due to the sideband boundary variation results in a systematic error on $BR(B_J^* \to B^*\pi)$ of $^{+0.076}_{-0.057}$.

- To account for any uncertainties arising from a wrongly simulated tracking resolution, the reconstructed track parameters are smeared by $\pm 10\%$ in the Monte Carlo. The resulting difference observed for $BR(B_J^* \to B^*\pi)$ is smaller than ± 0.010.

- The cuts of the signal pion selection have been varied. From the maximal deviations observed an error on $\mathrm{BR}(\mathrm{B}_J^* \to \mathrm{B}^*\pi)$ of $^{+0.042}_{-0.048}$ is derived.

- The cut on $\mathcal{W}(\mathrm{B}^*)$ has been varied. Only cuts producing samples with high statistics and with the ratio of signal-to-background ratios in the $\mathrm{B}\pi$ mass spectra of the B^*-enriched and B^*-depleted samples being close to 1 have been considered. The observed deviations in $\mathrm{BR}(\mathrm{B}_J^* \to \mathrm{B}^*\pi)$ do not exceed $^{+0.030}_{-0.043}$ which is taken as the systematic error due to the cut on $\mathcal{W}(\mathrm{B}^*)$.

- Reflections from B_{sJ}^* decays might influence the $\mathrm{BR}(\mathrm{B}_J^* \to \mathrm{B}^*\pi)$ result since a small fraction of kaons are misidentified as pions. As calculated from Monte Carlo, the amount of B_{sJ}^* seen in the B_J^* peaks is less than 4% for a B_{sJ}^* production rate consistent with [8]. Since the pion mass has been assumed to calculate the invariant mass, these misidentified $\mathrm{BK}^\pm$ combinations produce a broad peak around $M_{\mathrm{B}\pi} = 5.6\ \mathrm{GeV}/c^2$. The branching ratio $\mathrm{BR}(\mathrm{B}_{sJ}^* \to \mathrm{B}^*\mathrm{K})$ is varied from 0.2 to 1.0 in the simulation and the corresponding error on $\mathrm{BR}(\mathrm{B}_J^* \to \mathrm{B}^*\pi)$ is $^{+0.006}_{-0.026}$.

- Contributions from higher orbital or radial excitations of B mesons decaying to $\mathrm{B}^{(*)}\pi$ or $\mathrm{B}^{(*)}\pi\pi$ may be contained in the signal peaks of the B^*-enriched and the B^*-depleted samples. There is no experimental evidence for such states except for $\mathrm{B}^{(*)\prime} \to \mathrm{B}^{(*)}\pi\pi$ transitions [33]. Two Monte Carlo sets of radially-excited B mesons are generated in the decay channels $\mathrm{B}' \to \mathrm{B}\pi^+\pi^-$ and $\mathrm{B}^{*\prime} \to \mathrm{B}^*\pi^+\pi^-$. The states are produced with masses $M(\mathrm{B}') = 5.883\ \mathrm{GeV}/c^2$ and $M(\mathrm{B}^{*\prime}) = 5.898\ \mathrm{GeV}/c^2$ according to the theoretical expectation [3] and in agreement with [33]. The radial excitations are generated with widths of value zero, which is strongly supported by the experimental result [33]. According to the Monte Carlo, these $\mathrm{B}^{(*)\prime} \to \mathrm{B}^{(*)}\pi\pi$ decays cause a peak at 5.6 GeV/c^2 in the $\mathrm{B}\pi^\pm$ mass distributions. With the total B' production rate observed in [33], the B_J^* peak of Figure 6 does not contain more than 3% $\mathrm{B}^{(*)\prime}$ transitions. Although the production rates for B' and $\mathrm{B}^{*\prime}$ are expected to be rather similar, the fraction of $\mathrm{B}^{*\prime}$ of both radial excitations is varied from 0.3 to 0.7. The described estimation of $\mathrm{B}^{(*)\prime}$ contribution results in an additional error on $\mathrm{BR}(\mathrm{B}_J^* \to \mathrm{B}^*\pi)$ of $^{+0.000}_{-0.017}$.

- The whole analysis is repeated using conversion photons only and calorimeter photons only. The obtained branching ratio results and the $\mathrm{B}_J^* \to \mathrm{B}^*\pi^\pm$ and $\mathrm{B}_J^* \to \mathrm{B}\pi^\pm$ mass distributions are in agreement with each other and with the total sample.

- Different cuts on $\mathcal{B}_{\mathrm{event}}$ are applied and the whole analysis is repeated, resulting in a change of the b purity from 92% to 98%. No systematic deviation of $\mathrm{BR}(\mathrm{B}_J^* \to \mathrm{B}^*\pi)$ is observed.

- A neural network has been trained to replace the weight $\mathcal{W}(\mathrm{B}^*)$ obtained from the Monte Carlo purity parameterisation. The neural network output is strongly correlated with the weight $\mathcal{W}(\mathrm{B}^*)$ but does not improve the B^*/B separation.

9 Summary and conclusion

We have analysed orbitally-excited mesons in their dominant decay channels $\mathrm{B}_J^* \to \mathrm{B}^*\pi^\pm$ and $\mathrm{B}_J^* \to \mathrm{B}\pi^\pm$. We present a method of statistical separation of these two transitions. This method guarantees a good control of the combinatorial $\mathrm{B}\pi$ background which is the dominating

uncertainty in standard B_J^* analyses. For the first time we measure the branching ratio of orbitally-excited B mesons decaying into B^*. The result is

$$BR(B_J^* \to B^*\pi) = 0.85^{+0.26}_{-0.27} \pm 0.12\,,$$

where the first error is statistical and the second systematic. The measurement does not depend on any specific theoretical model. It is in agreement with theoretical predictions and the measured B^* and B_J^* production rates at LEP.

References

[1] M. Volonshin and M. Shifman, Sov. J. Nucl. Phys. 45 (1987) 292;
M. Volonshin and M. Shifman, Sov. J. Nucl. Phys. 47 (1988) 511;
S. Nussinov and W. Wetzel, Phys. Rev. D36 (1987) 130;
N. Isgur and M.B. Wise, Phys. Lett. B232 (1989) 113;
N. Isgur and M.B. Wise, Phys. Lett. B237 (1990) 527;
N. Isgur and M.B. Wise, Phys. Rev. Lett. 66 (1991) 1130;
E. Eichten and B. Hill, Phys. Lett. B234 (1990) 511;
B. Grinstein, Nucl. Phys. B339 (1990) 253;
H. Georgi, Phys. Lett. B240 (1990) 447;
A. Falk, H. Georgi, B. Grinstein, M. Wise, Nucl. Phys. B343 (1990) 1;
J.D. Bjorken, I. David, J. Taron, Nucl. Phys. B371 (1990) 111.

[2] Particle Data Group, C. Caso et al., Eur. Phys. J. C3 (1998) 1.

[3] D. Ebert, V.O. Galkin, R.N. Faustov, Phys. Rev. D57 (1998) 5663;
Erratum Phys. Rev. D59 (1999) 019902.

[4] S. Godfrey and R. Kokoski, Phys. Rev. D43 (1991) 1679.

[5] E.J. Eichten, C.T. Hill, C. Quigg, Phys. Rev. Lett. 71 (1993) 4116;
E.J. Eichten, C.T. Hill, C. Quigg, FERMILAB-CONF-94-117-T, May 1994.

[6] S. Godfrey and N. Isgur, Phys. Rev. D32 (1985) 189;
M. Gronau and J. Rosner, Phys. Rev. D49 (1994) 254;
N. Gupta and J.M. Johnson, Phys. Rev. D51 (1994) 168;
A.F. Falk and T.Mehen, Phys. Rev. D53 (1996) 231;
Y.-B. Dai and S.-L. Zhu, Phys. Rev. D58 (1998) 074009;
Y.-B. Dai, C.-S. Huang, M.-Q. Huang, H.-Y. Jin, C. Liu, Phys. Rev. D58 (1998) 094032.

[7] N. Isgur, Phys. Rev. D57 (1998) 4041.

[8] OPAL collaboration, G. Alexander et al., Z. Phys. C66 (1995) 19.

[9] DELPHI collaboration, P. Abreu et al., Phys. Lett. B345 (1995) 598.

[10] ALEPH collaboration, D. Buskulic et al., Z. Phys. C69 (1996) 393.

[11] ALEPH collaboration, R. Barate et al., Phys. Lett. B425 (1998) 215.

[12] P.P. Allport et al., Nucl. Instr. Meth. A346 (1994) 476.

[13] OPAL collaboration, K. Ahmet et al., Nucl. Instr. Meth. A305 (1991) 275;
P.P. Allport et al., Nucl. Instr. Meth. A324 (1993) 34.

[14] OPAL collaboration, G. Alexander et al., Z. Phys. C52 (1991) 175.

[15] T. Sjöstrand, Comp. Phys. Comm. 82 (1994) 74.

[16] OPAL collaboration, G. Alexander et al., Z. Phys. C69 (1996) 543.

[17] C. Peterson, D. Schlatter, I. Schmitt and P. Zerwas, Phys. Rev. D27 (1983) 105.

[18] J. Allison et al., Nucl. Instr. Meth. A317 (1992) 47.

[19] OPAL collaboration, K. Ackerstaff et al., Z. Phys. C74 (1997) 413.

[20] N. Brown and W.J. Stirling, Phys. Lett. B252 (1990) 657;
S. Bethke, Z. Kunszt, D. Soper and W.J. Stirling, Nucl. Phys. B370 (1992) 310;
S. Catani et al., Phys. Lett. B269 (1991) 432;
N. Brown and W.J. Stirling, Z. Phys. C53 (1992) 629.

[21] OPAL Collaboration, K. Ackerstaff et al., Eur. Phys. J. C2 (1998) 213.

[22] OPAL Collaboration, G. Abbiendi et al., Eur. Phys. J. C7 (1999) 407.

[23] OPAL collaboration, R. Akers et al., Z. Phys. C63 (1994) 197.

[24] The neural networks were trained using JETNET 3:
C. Peterson, T. Rögnvaldsson and L. Lönnblad, Comp. Phys. Comm. 81 (1994) 185.

[25] A similar neural network has already been used in:
OPAL Collaboration, G. Abbiendi et al., Eur. Phys. J. C8 (1999) 217.

[26] OPAL collaboration, K. Ackerstaff et al., Eur. Phys. J. C5 (1998) 411;
OPAL collaboration, K. Ackerstaff et al., Z. Phys. C74 (1997) 413;
OPAL collaboration, G. Alexander et al., Z. Phys. C73 (1997) 587;
OPAL collaboration, G. Alexander et al., Z. Phys. C70 (1996) 357.

[27] OPAL collaboration, K. Ackerstaff et al., Eur. Phys. J. C5 (1998) 411.

[28] OPAL collaboration, R. Akers et al., Phys. Lett. B316 (1993) 435.

[29] G. Eigen, Int. J. Mod. Phys. A12 (1997) 3909;
R. Kokoski and N. Isgur, Phys. Rev. D35 (1987) 907

[30] A.F. Falk and M.E. Peskin, Phys. Rev. DD49 (1994) 3320.

[31] OPAL collaboration, G. Abbiendi et al., Eur. Phys. J. C8 (1999) 573.

[32] DELPHI collaboration, P. Abreu et al., Phys. Lett. B425 (1998) 399;
L3 collaboration, M. Acciari et al., Phys. Lett. B416 (1998) 220;
OPAL collaboration, R. Akers et al., Z. Phys. C61 (1994) 209.

[33] G. Eigen, Int. J. Mod. Phys. A12 (1997) 3909;
M.-L. Andrieux, Nucl. Phys. B Proc. Suppl. 55A (1997) 51.

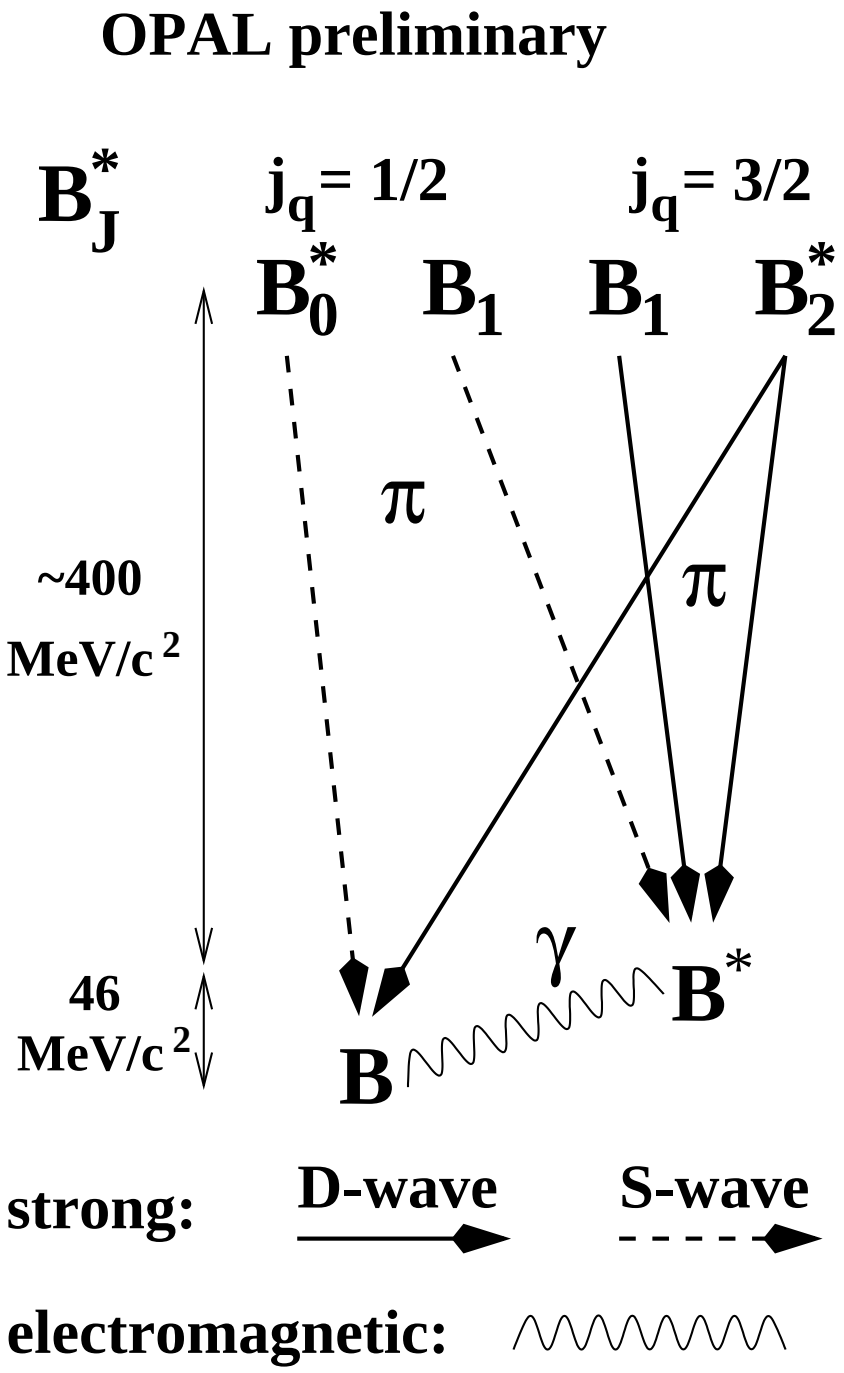

Figure 1: The four B^*_J states and their dominant decays to the ground state doublet (B, B^*). Strong decays via single pion emission are indicated as solid (D-wave) and dashed (S-wave) lines. The B^* decays radiatively because of the small B^*–B mass splitting.

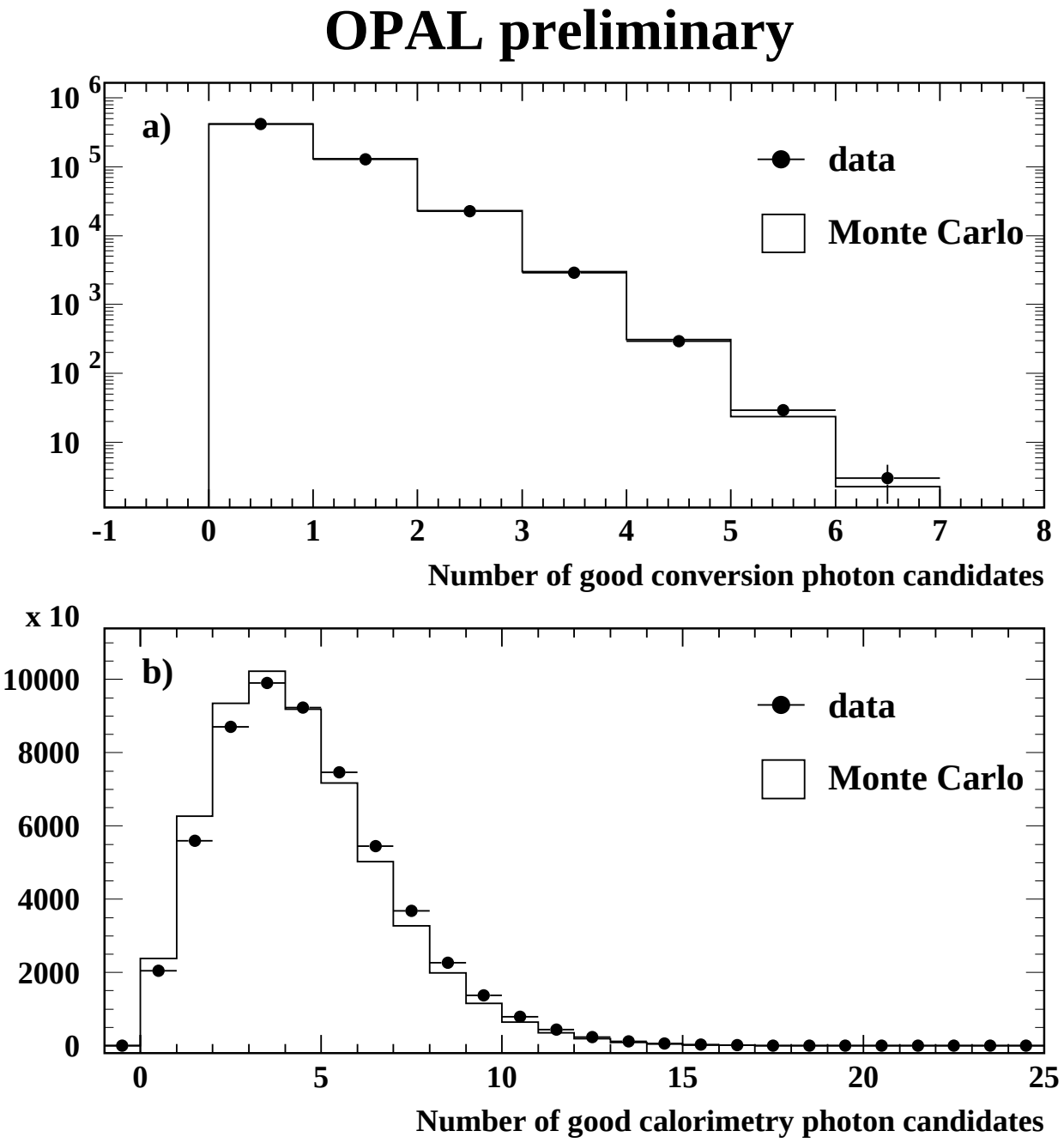

Figure 2: a) The number of good conversion photon candidates per B candidate observed in data and Monte Carlo. b) The number of good calorimeter photon candidates per B candidate observed in data and Monte Carlo. For the analysis, the Monte Carlo distribution of the latter is reweighted to the data distribution.

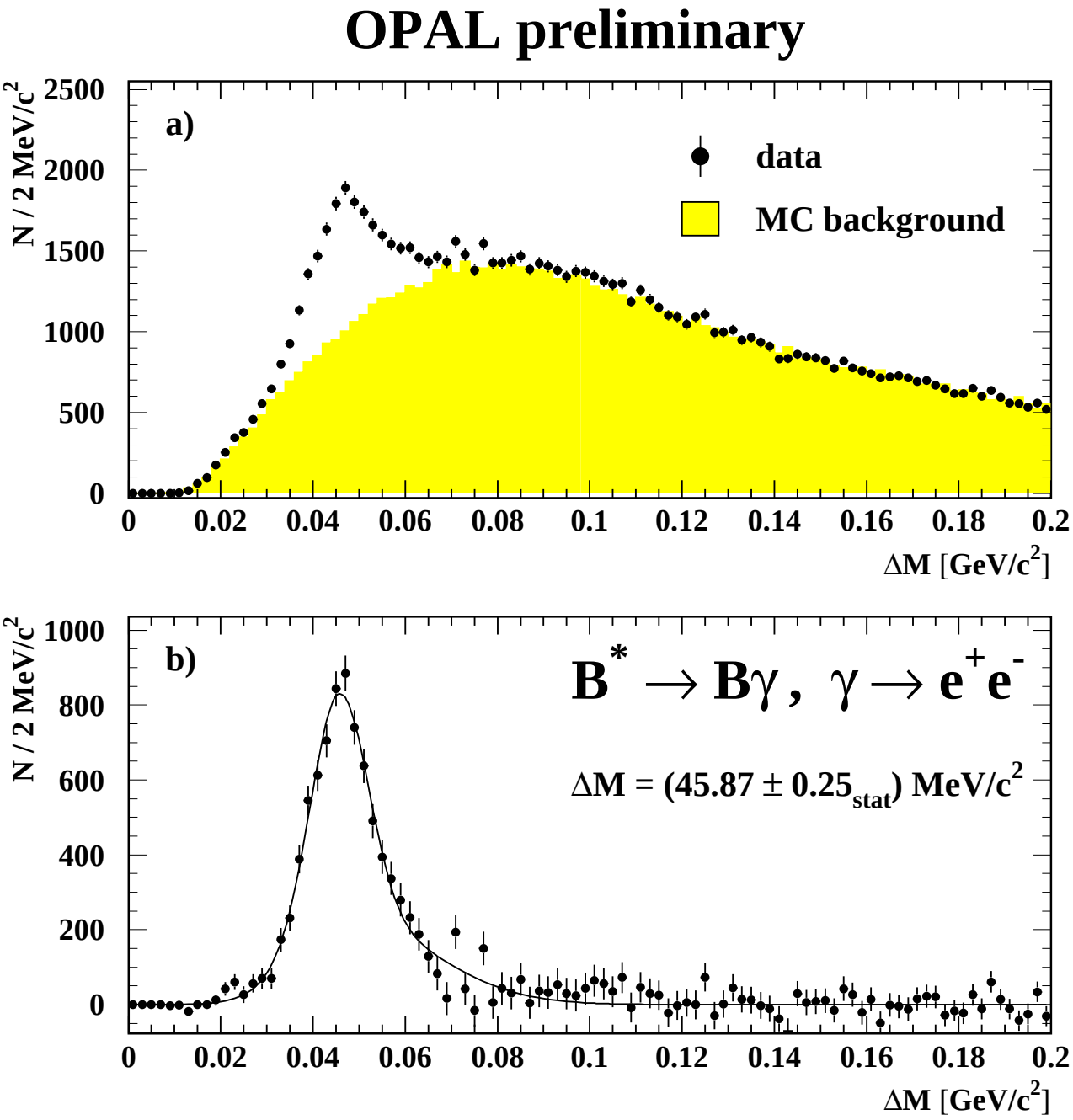

Figure 3: a) The $\Delta M = M_{\mathrm{B}\gamma} - M_{\mathrm{B}}$ mass distribution of the conversion photon sample. The background is estimated from Monte Carlo simulation and normalised to the data distribution in the sideband region 0.09 GeV/c^2 $< \Delta M <$ 0.20 GeV/c^2. b) The corresponding background subtracted signal. The fit function used for the signal is described in the text on page 8.

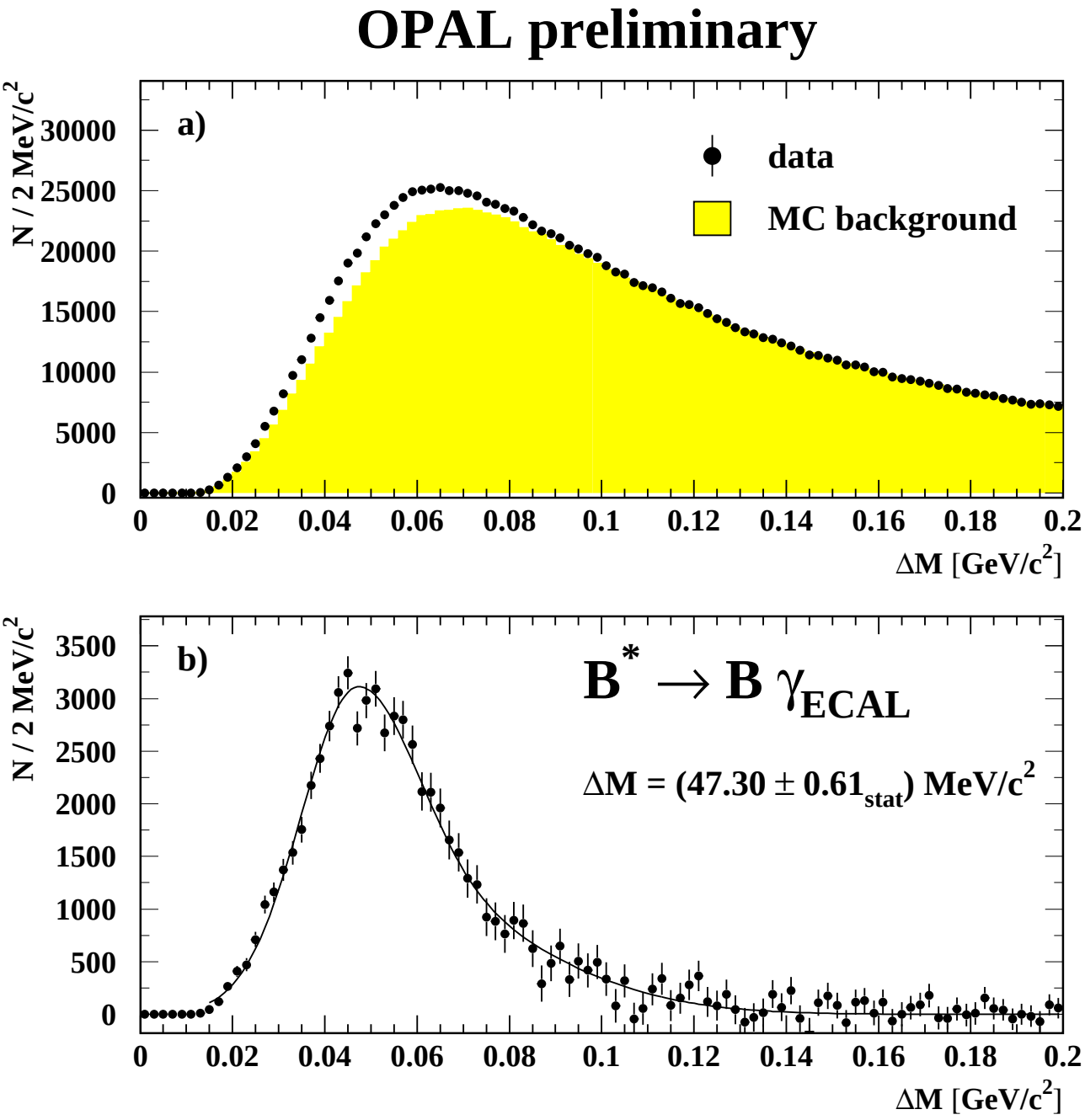

Figure 4: a) The $\Delta M = M_{\mathrm{B}\gamma} - M_{\mathrm{B}}$ mass distribution of photons reconstructed in the electromagnetic calorimeter. The background is estimated from the Monte Carlo simulation and normalised to the data distribution in the sideband region 0.10 GeV/c^2 $< \Delta M <$ 0.20 GeV/c^2. Although the resolution is poor compared to the conversion photon sample, an excess of entries in the data distribution around 46 MeV/c^2 is clearly visible. b) The corresponding background subtracted signal. The fit function is described in the text on page 8.

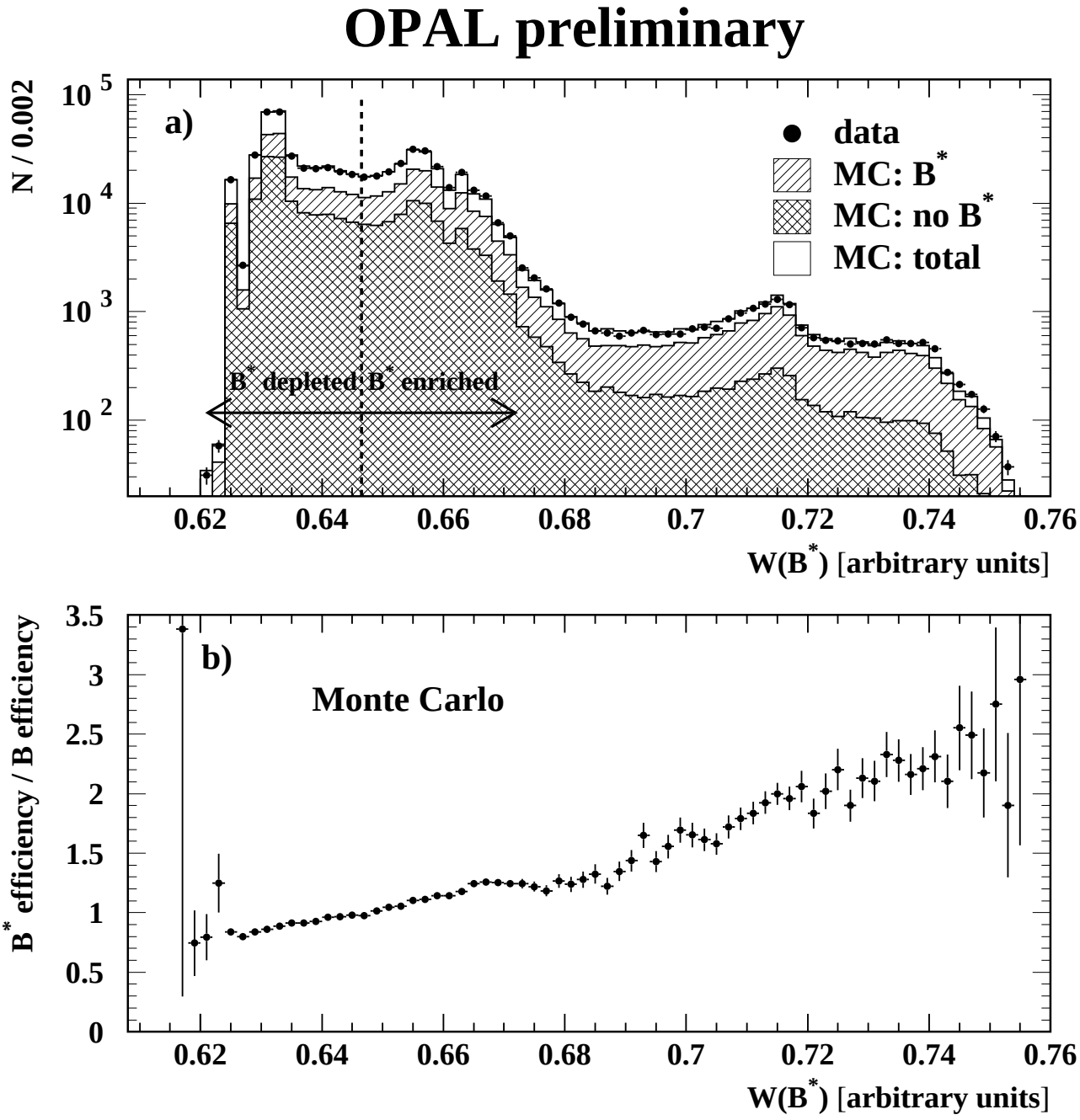

Figure 5: a) The $\mathcal{W}(\mathrm{B}^*)$ distribution for data with the corresponding Monte Carlo histograms indicating the number of B candidates with a B^* parent and no B^* parent. The dotted line gives the boundary between the B^*-enriched and B^*-depleted samples. b) The ratio of the efficiency to reconstruct a B meson with a B^* parent over the efficiency to reconstruct a B meson without a B^* parent versus the weight $\mathcal{W}(\mathrm{B}^*)$ calculated from simulated data.

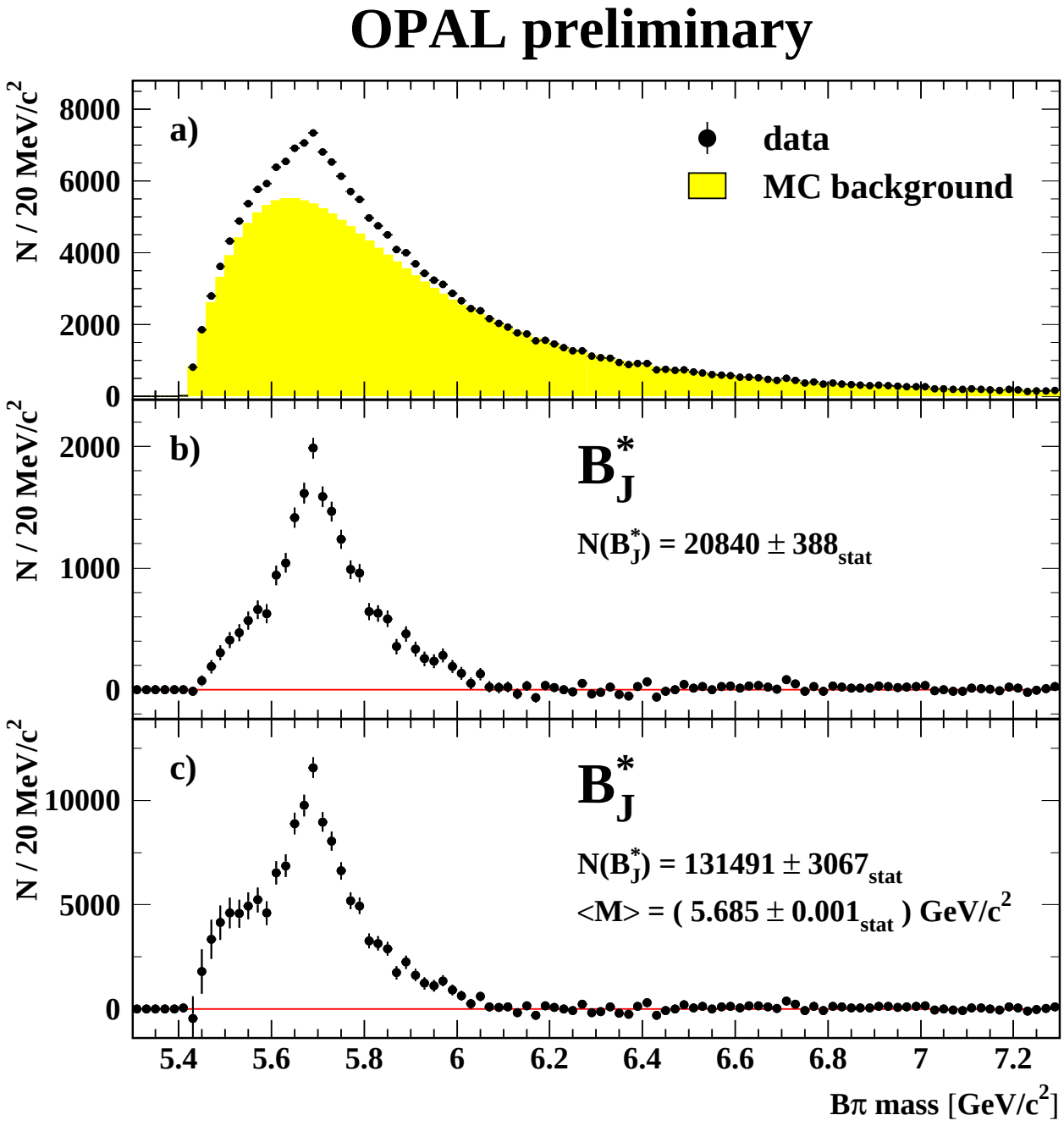

Figure 6: a) The $B\pi^{\pm}$ mass distribution for data. The shaded histogram indicates a fit to the corrected Monte Carlo background using a reweighting method described in Subsection 8.2. The function used for the fit is described in the text on page 11. b) The Monte Carlo background-subtracted signal. c) The efficiency-corrected B_J^* signal. The observed structure of the B_J^* signal suggests a superposition of several different states.

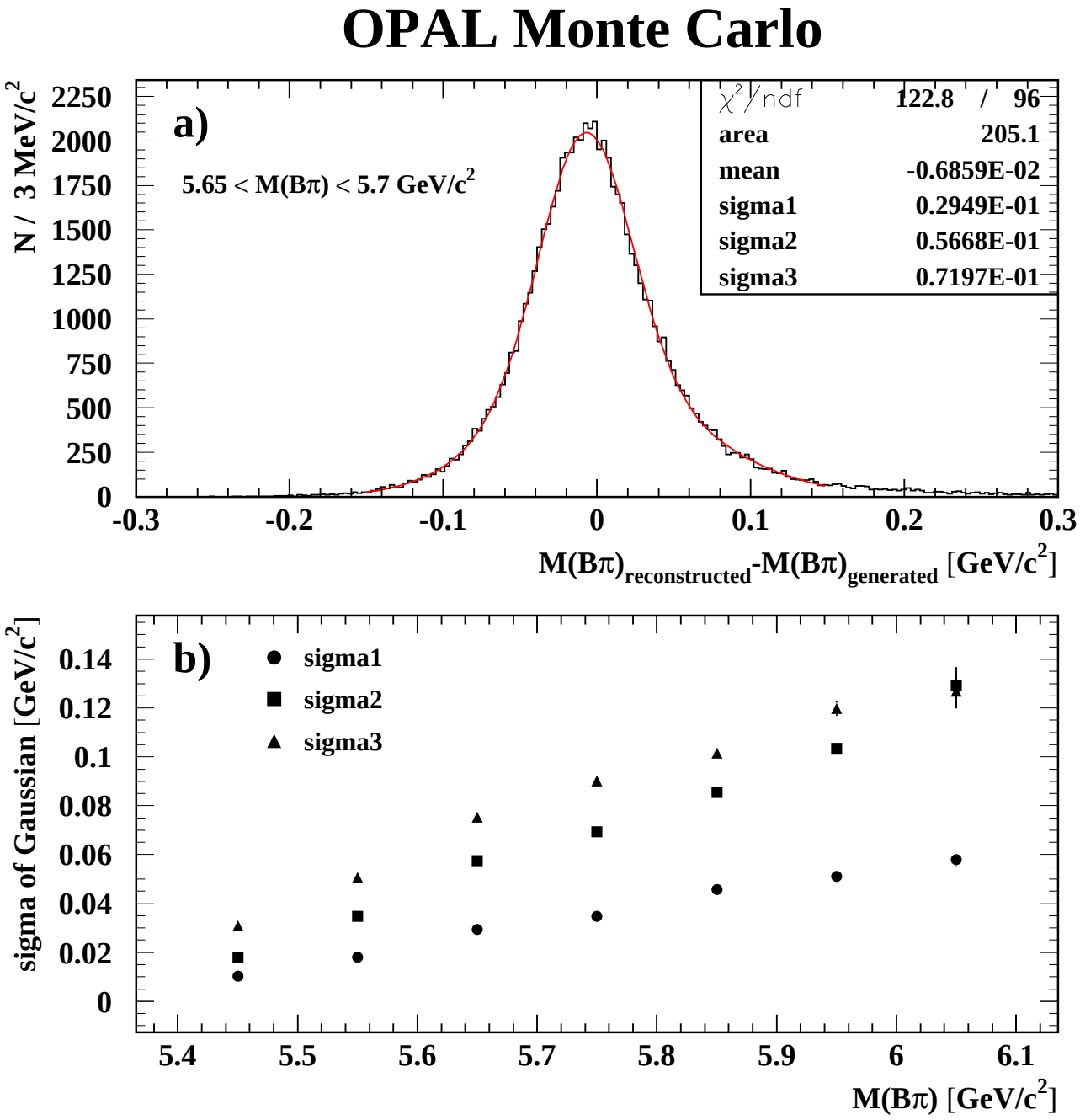

Figure 7: a) Monte Carlo $M_{\mathrm{B}\pi}$ resolution of B_J^* decaying to $\mathrm{B}^{(*)}\pi^{\pm}$ in the mass region 5.65 GeV/c^2 < $M(\mathrm{B}\pi)$ < 5.70 GeV/c^2. The fit function is the sum of two Gaussians both constrained to the same mean value. Sigma1 is the standard deviation of the narrow Gaussian and sigma2 (sigma3) corresponds to the left (right) standard deviation of the asymmetric broad Gaussian. b) The linear dependence of the width of the resolution function on $M_{\mathrm{B}\pi}$ is shown for each sigma in the B_J^* signal region.

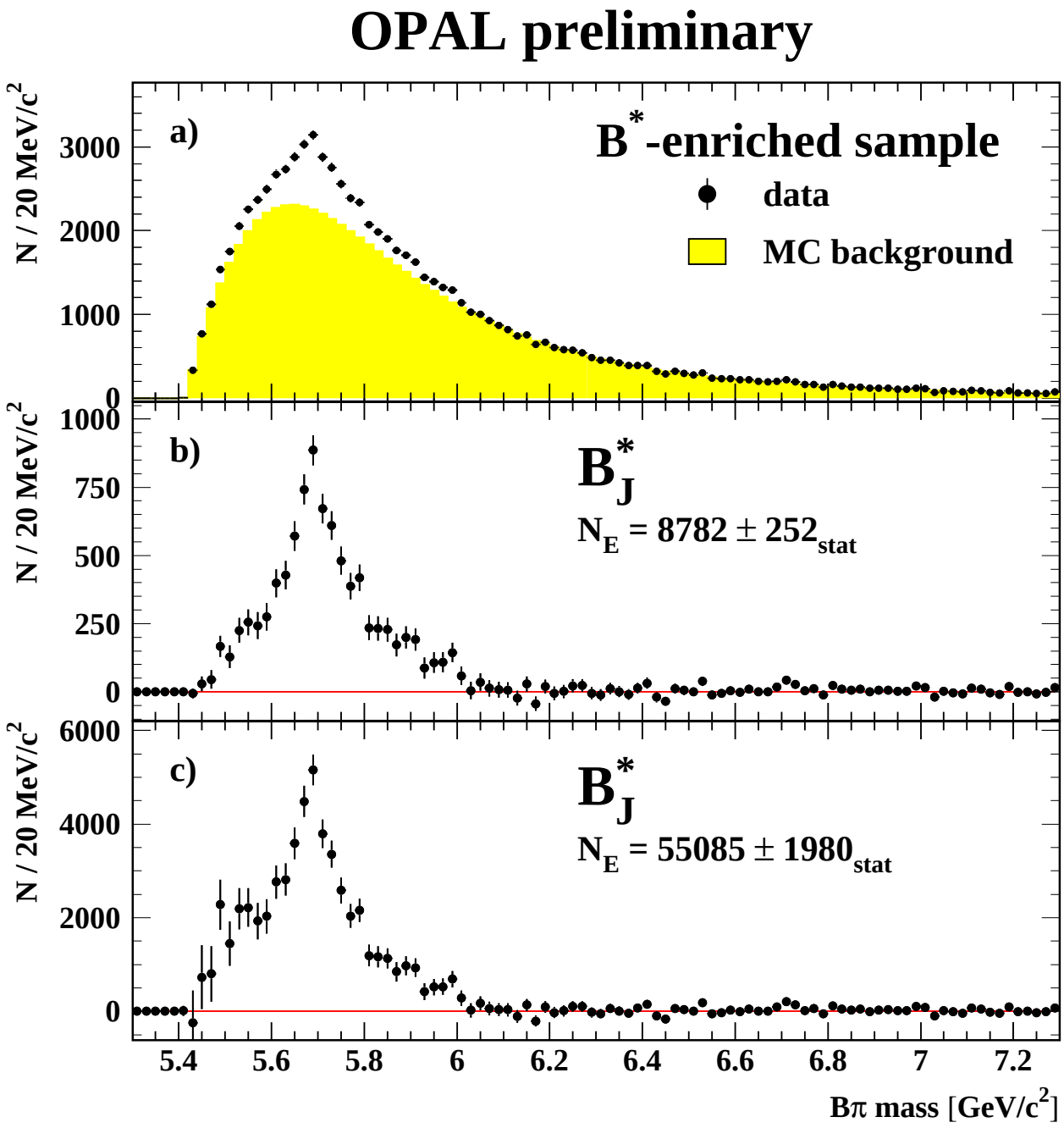

Figure 8: a) The $B\pi^{\pm}$ mass distribution of the sample enriched in the decay $B^*_J \to B^*\pi^{\pm}$ in data. The shaded histogram indicates a fit to the corrected Monte Carlo background using a reweighting method described in Subsection 8.2. b) The Monte Carlo signal distribution after background subtraction. c) The efficiency-corrected signal.

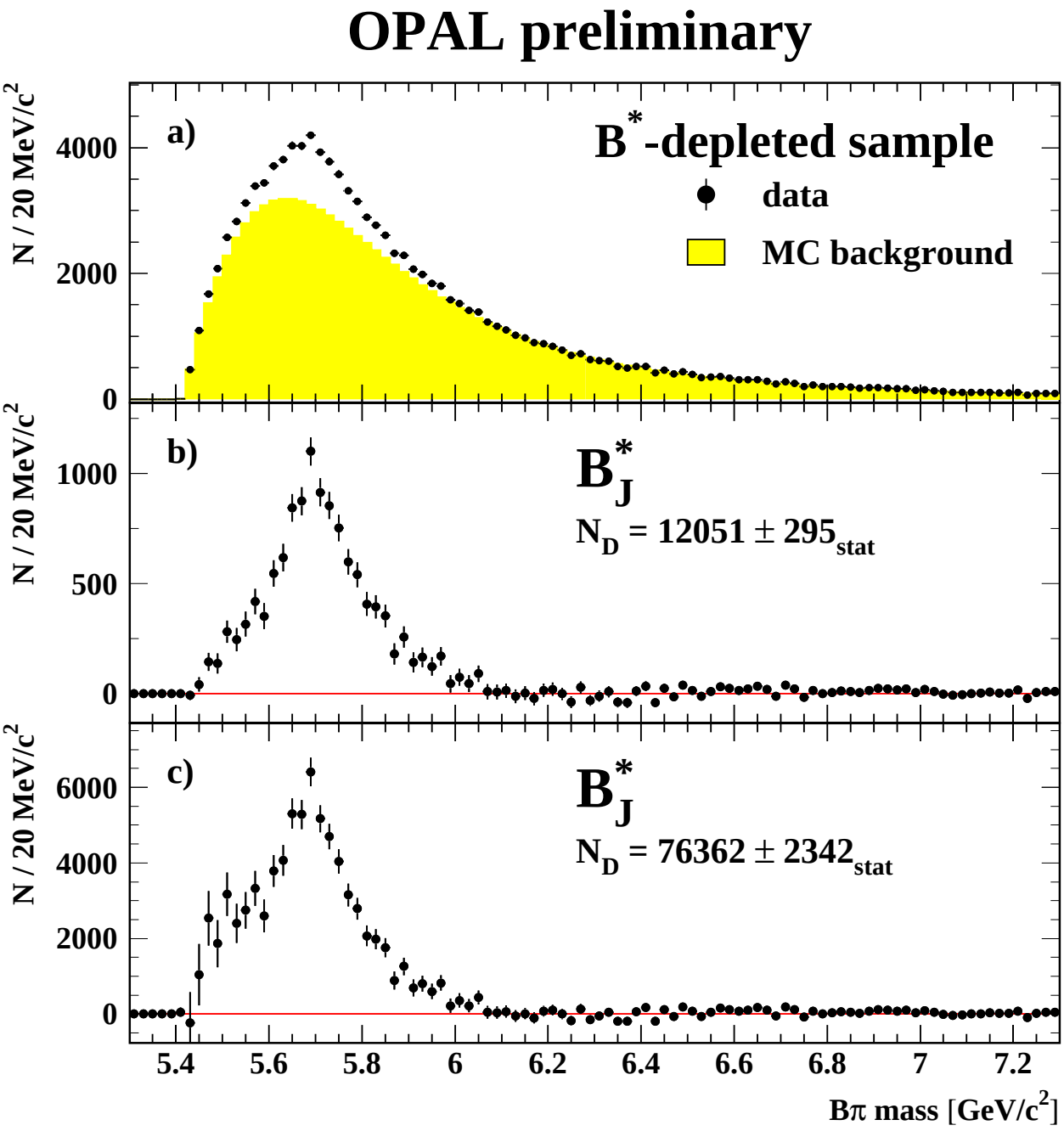

Figure 9: a) The $B\pi^{\pm}$ mass distribution of the sample depleted in the decay $B^*_J \to B^*\pi^{\pm}$ in data. The shaded histogram indicates a fit to the corrected Monte Carlo background using a reweighting method described in Subsection 8.2. b) The Monte Carlo signal after background subtraction. c) The efficiency-corrected signal.

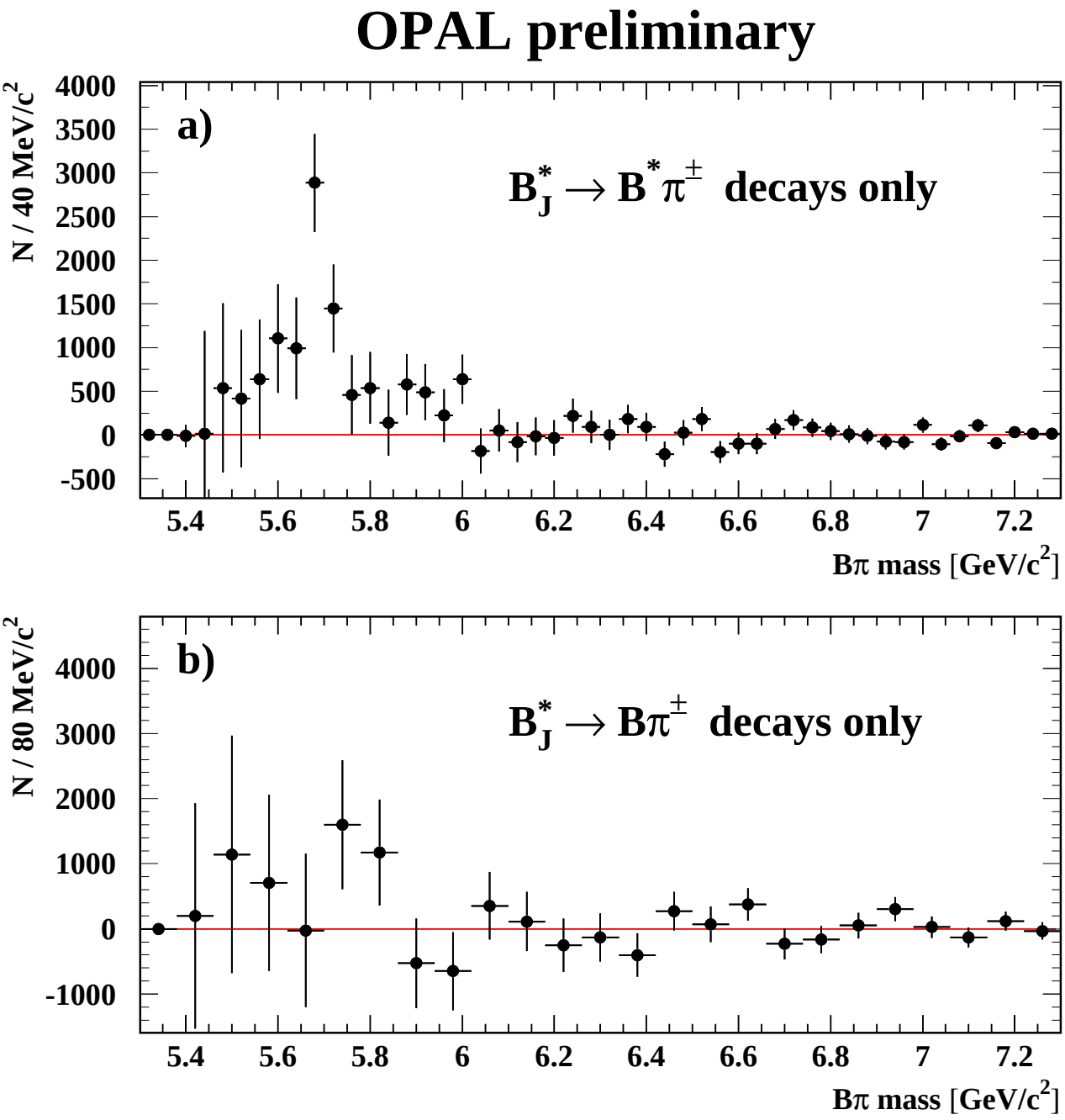

Figure 10: a) The efficiency-corrected $B\pi^\pm$ mass distribution of $B_J^* \to B^*\pi^\pm$ transitions seen in data. A clear peak is visible at 5.7 GeV/c^2. The structure is unlikely to stem from a single state. b) The efficiency-corrected $B\pi^\pm$ mass distribution of $B_J^* \to B\pi^\pm$ transitions seen in data. A 2.2σ excess is observed around 5.8 GeV/c^2.

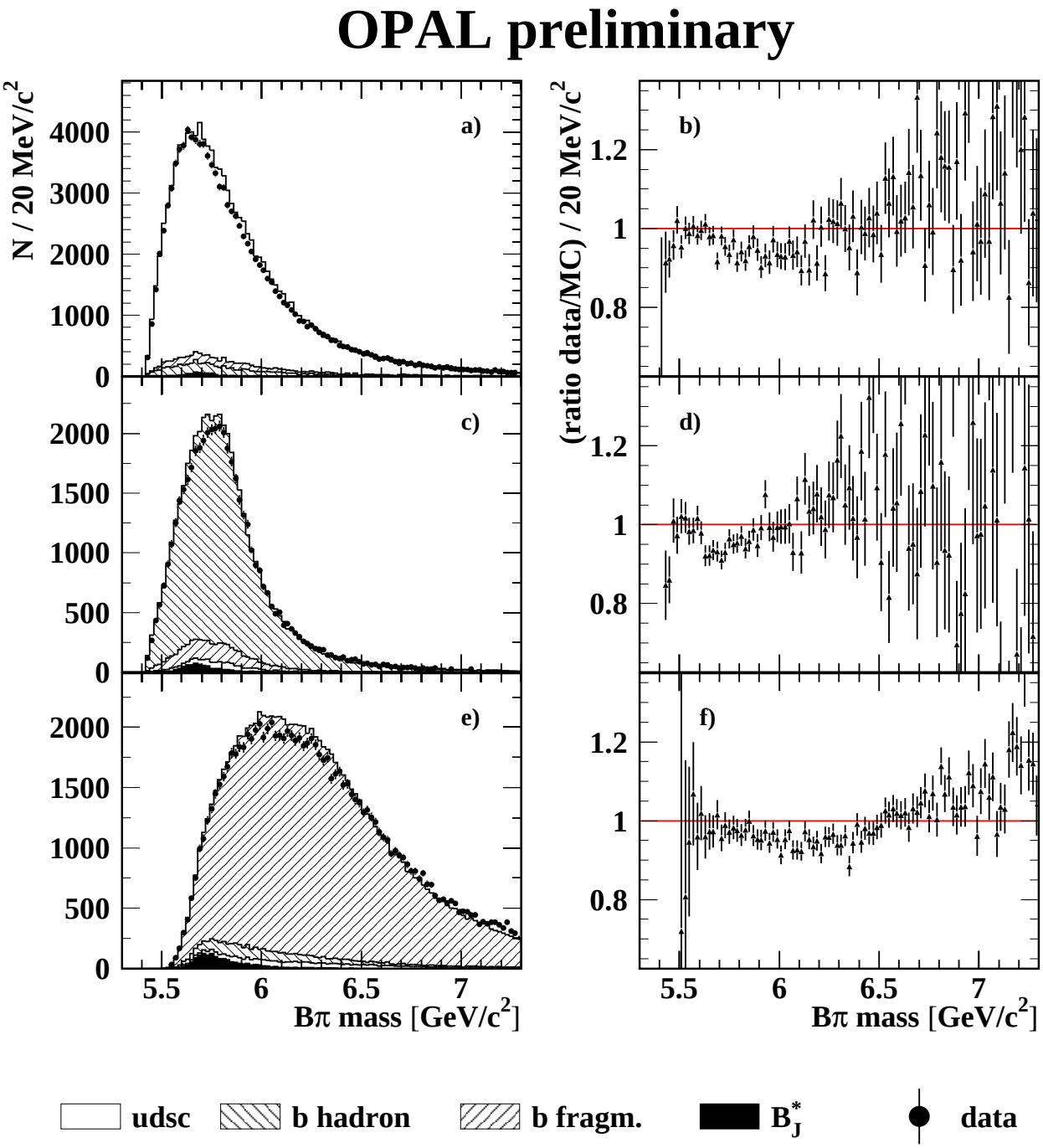

Figure 11: The $B\pi^{\pm}$ mass distributions of data and Monte Carlo for each of the three test samples (left side) and the corresponding bin-by-bin ratio of the mass distributions (right side). a)+b) Light and charm quark sample, c)+d) b hadron decay sample, e)+f) b fragmentation sample.